Engineering Geology 182 (2014) 158–181

Contents lists available at ScienceDirect

Engineering Geology

journal homepage: www.elsevier.com/locate/enggeo

# Initiation, movement, and run-out of the giant Tsaoling landslide — What can we learn from a simple rigid block model and a velocity–displacement dependent friction law?

Che-Ming Yang [a], Wei-Lun Yu [a], Jia-Jyun Dong [a,*], Chih-Yu Kuo [b], Toshihiko Shimamoto [c], Chyi-Tyi Lee [a], Tetsuhiro Togo [d], Yuki Miyamoto [e]

[a] Graduate Institute of Applied Geology, National Central University, Taiwan
[b] Research Center for Applied Sciences, Academia Sinica, Taiwan
[c] State Key Laboratory of Earthquake Dynamics, Institute of Geology, China Earthquake Administration, China
[d] Seismotectonics Research Group, Institute of Earthquake and Volcano Geology, National Institute of Advanced Industrial Science and Technology, Japan
[e] Kimitsu Works, Nippon Steel & Sumitomo Metal Corpration, Japan

ARTICLE INFO

*Article history:*
Accepted 10 August 2014
Available online 19 August 2014

*Keywords:*
Tsaoling landslide
Chi-Chi earthquake
Newmark analysis
High-velocity friction
Rigid-block landslide model
Rotary-shear friction experiment

ABSTRACT

Tsaoling landslide is the largest and best documented landslide among several large landslides induced by the 1999 Taiwan Chi-Chi earthquake. Pliocene sedimentary rocks of about 125 $Mm^3$ in volume slid along very flat bedding planes dipping by 14° with an average speed of 35–40 m/s for about 1650 m, before hitting the bank of the Chinshui River during the landslide. Detailed analysis of DTMs before and after the earthquake using a GIS software leads to an accurate determination of the locations of the centroids of landslide mass, revealing the horizontal and vertical displacements of the 2524 m and 524 m, respectively. Those displacements and landslide mass give an apparent friction coefficient of 0.21 and the release of the potential energy of $1.6 \times 10^{15}$ J. We conducted rotary-shear high-velocity friction experiments on fault gouge from bedding-parallel faults under semi-wet conditions and at 3 MPa normal stress corresponding to the overburden pressure of the landslide mass. We also compiled reported data on the frictional properties on shale powders and fault gouge from the landslide site under both dry and wet conditions, and proposed a velocity–displacement dependent friction law that can describe most experimental data. Newmark analysis of landslide motion with six scenarios for different landslide materials and conditions, assuming a simple rigid block sliding and using measured frictional parameters, revealed that the landslide did not occur with dry frictional properties, and that the landslide occurred at 38–39 s with accumulated displacements of 0.62 m–1.09 m and reached at the river bank at 82–87 s after the generation of Chi-Chi earthquake at its epicenter. Those timings are consistent with high-frequency signals at 32–40 s and at 76 s recorded at a nearby seismic station and with a survivor's witness that the landslide initiated 10 s after he felt strong ground motion, possible S wave arrival at 25.2 s. Slip-weakening is essential in initiating the landslide and low friction coefficient (0.08–0.1) allowed high-speed of the landslide possible. The landslide was caused by a few peaks of northeast-oriented strong accelerations of the ground motion. Frictional work during the sliding of the landslide mass was estimated to be of about 23% of potential energy, and the rest of the released energy is likely to have been consumed during the stopping phase of the landslide after hitting the river bank in complex processes such as fragmentation, heat dissipation, and spreading of the landslide deposits.

© 2014 The Authors. Published by Elsevier B.V. This is an open access article under the CC BY license (http://creativecommons.org/licenses/by/4.0/).

## 1. Introduction

Giant landslides frequently induce catastrophic hazards. A key issue for mitigating landslide hazards is how to predict the processes of triggering, movement, and deposition of a landslide mass. Numerical simulations are widely used approach to predict the kinematics of large landslides that have fast sliding velocities and long run-out distances (e.g., Campbell, 1989; Cleary and Campbell, 1993; Campbell et al., 1995; Hungr, 1995; Hungr et al., 2001; Legros, 2002; Crosta et al., 2003; Tang et al., 2009; Wu and Chen, 2011).However, it is not easy, if not impossible, to determine the appropriate parameters for the numerical model. In the case of high-speed rock sliding, frictional properties along the sliding surface at high velocities and large shear displacements are the most important factor that dominates the kinematics of large landslides (e.g., Voight and Faust, 1982; Tika and Hutchinson, 1999; Chang et al., 2005). Dong et al. (2009) showed that the kinematics

* Corresponding author at: 300, Jhongda Rd., Jhongli, Taoyuan 32001, Taiwan. Tel./fax: +886 3 4224114.
*E-mail address:* jjdong@geo.ncu.edu.tw (J.-J. Dong).

http://dx.doi.org/10.1016/j.enggeo.2014.08.008
0013-7952/© 2014 The Authors. Published by Elsevier B.V. This is an open access article under the CC BY license (http://creativecommons.org/licenses/by/4.0/).

of landslides can be depicted well using a simple rigid block model that incorporates a velocity-dependent friction law. This paper attempts to combine laboratory studies on the high-velocity frictional properties of sliding surface and a Newmark analysis of landslide motion, for a realistic prediction of the Tsaoling landslide. This landslide is the largest and best-documented landslide among several large landslides triggering by the 1999 Taiwan Chi-Chi earthquake ($M_w = 7.6$) with its volume of about 125 $Mm^3$ (Hung, 2000; Weissel and Stark, 2001; Hung et al., 2002; Chigira et al., 2003; Wang et al., 2003; Chen et al., 2004; Chang et al., 2005; Chen et al., 2005, 2006; Kuo et al., 2009; Miyamoto et al., 2009; Tang et al., 2009; Wu and Chen, 2009, 2011; Chang et al., 2013; Kuo et al., 2013; Chen et al., 2014; Togo et al., 2014). In particular, a landslide mass of the Pliocene Cholan Formation (about 140 m in thickness) slid along very flat bedding planes within alternated fine sandstone and shale beds dipping by 14° on the southern slope of the Tsaoling Mountain, as we discuss Figs. 1–3 later. Thus, the geometry and kinematics of the Tsaoling landslide are ideal for a simple rigid-block analysis with frictional properties, using the Newmark method (Newmark, 1965).

After sliding for about 800 m along bedding planes dipping 14° and then for about the same distance along steeper slope dipping about 20°, the Tsaoling landslide mass hit a southwestern bank of Chinshui river and deposited over Mt. Daoqiaoshan of about 60 m in height (e.g., Chen et al., 2004; Chigira et al., 2003; Chen et al., 2006; Tang et al., 2009). A strong motion seismometer at station CHY080 (TWD97: X = 217,073, Y = 2,610,450, EL. 840 m) located at about 800 m to the north from the center of the Tsaoling landslide mass recorded high-frequency signals starting at 75.8 s after the generation of Chi-Chi earthquake and lasting for about 1 s. Kuo et al. (2009) interpreted that the signals are due to the impact of the landslide mass to the river bank. Moreover, thirty-nine people in a village on the landslide mass slide with the landslide and seven of them survived (Chen et al., 2004). We found a survivor who witnessed that the landslide motion initiated about 10 s after he felt "strong shaking", possibly due to the S wave arrival (25.2 s after the Chi-Chi earthquake). Finally, Chen et al. (2014) found earlier high-frequency signals in the seismic record and proposed that the Tsaoling landslide started at 12–16 s after the S-wave arrival. Those information yields an average speed of landslide motion of 22–42 m/s, or a typical speed of around 30 m/s (Togo et al., 2014, Supplementary Information S1). Thus, the initiation and motion of the Tsaoling landslide are documented well and any model can be tested against those constraints from the seismic records and a survivor's witness.

Traditional direct shear tests at low slip rates yielded a peak friction angle of 39° (friction coefficient of 0.8) and an average residual friction angle of 23° (friction coefficient of 0.43) on the rocks from the Tsaoling landslide (WRA, 2000; Lee, 2001; Towhata et al., 2001). Huang et al. (2001) conducted a Newmark analysis of the Tsaoling landslide using those values, but the landslide motion stopped upon the reduction of the seismic ground motion. Based on the pseudostatic analysis, Chen et al. (2004) inferred that the Tsaoling landslide could be triggered by the Chi-Chi earthquake with a peak friction angle of 30° (equivalent to a friction coefficient of 0.58). A serious problem in those analyses with the results from the direct shear tests is that the landslide motion stops upon a reduction of seismic ground motion because the residual friction angle (23°) is greater than the dipping angle of the slope (14°). On the other hand, Kuo et al. (2009) used the continuum model of hydraulic flow, SHALTOP2D, which is based on the equations of Bouchut and Westdickenberg (2004) to simulate the dynamic motion of the Tsaoling landslide and obtain a calibrated friction coefficient of 0.09 (friction angle of 5°). Using the code PFC2D and parameters constrained by the final geometry of the landslide deposits, Tang et al. (2009) obtained a calibrated friction coefficient of 0.15 (friction angle of 8.5°). Furthermore, the apparent friction coefficient was calculated from the vertical fall height and the horizontal run-out distance (Heim, 1932; Scheidegger, 1975; Legros, 2002) to be approximately 0.21 (friction angle of 12°). Those friction angles allow runaway instability of the Tsaoling landslide along a slope with a dip angle of 14°. However, if the initial friction angle is as low as those values, the landslide mass could not stay along a flat surface in the first place. Hence, those analyses do not elucidate the triggering part of the Tsaoling landslide.

Thus, an essential process for triggering the Tsaoling landslide and for causing its high-speed motion is the marked slip-weakening from a high initial friction coefficient (high enough to keep the landslide mass on the slope) to a very low friction coefficient (low enough to allow high-speed

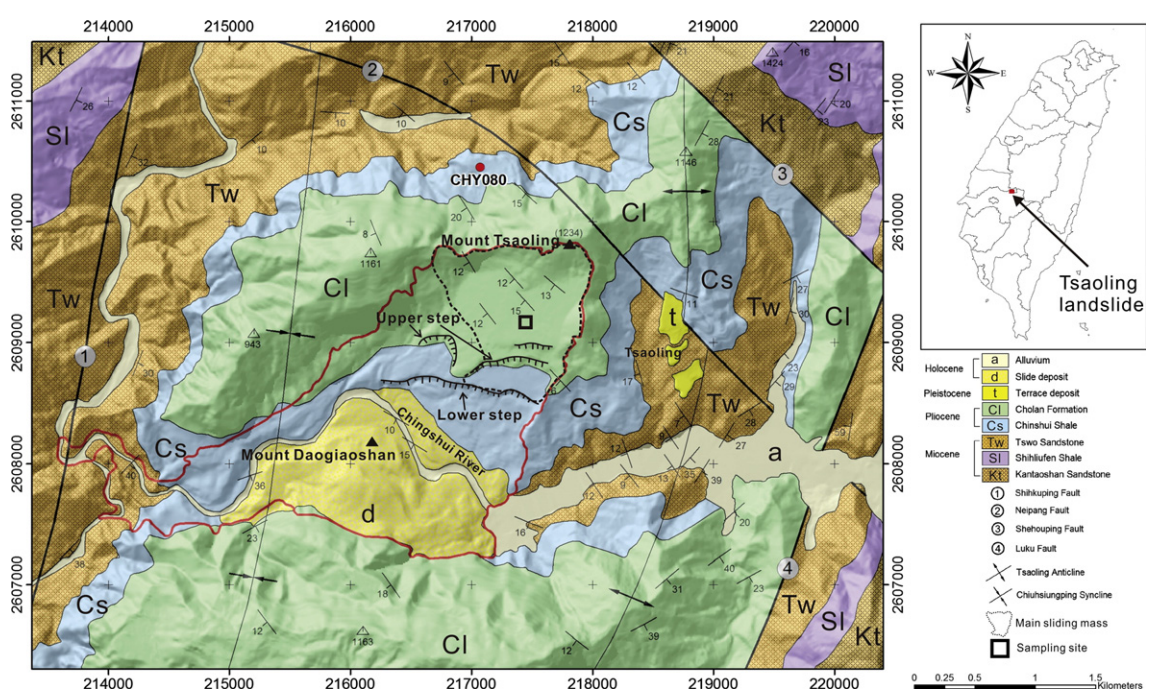


**Fig. 1.** Geological map of the Tsaoling landslide site (red curve) and the neighboring area. The strong motion station CHY080 is located north of the Tsaoling landslide (red circle). The location of the landslide is shown by a red square in the inset map of Taiwan.

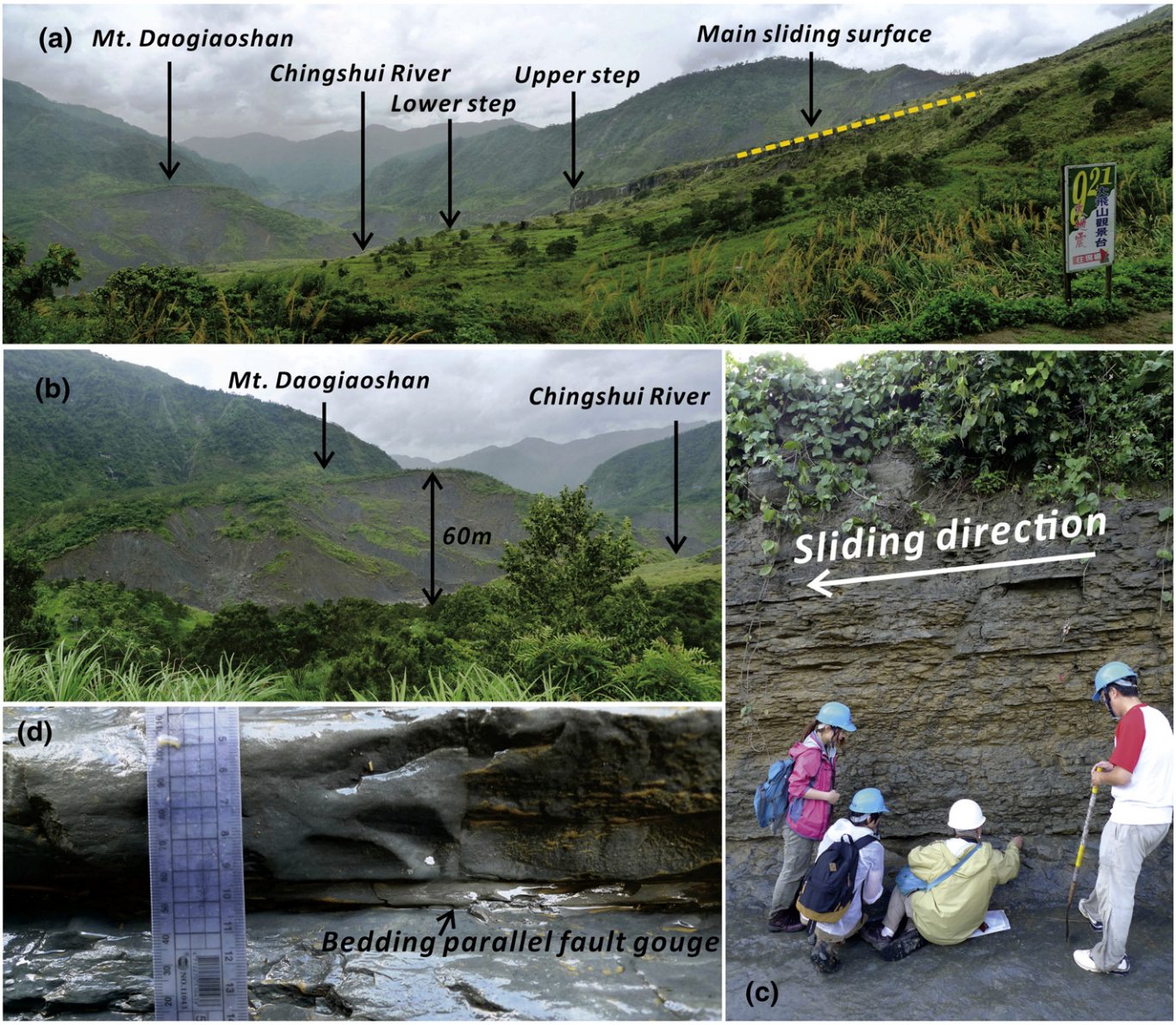


**Fig. 2.** Photographs showing (a) a side view of the Tsaoling landslide surface, (b) Mt. Daogiaoshan on the SW side of the Chingshui River, where the Tsaoling landslide mass was deposited, (c) sampling location of the gouge, and (d) a bedding-parallel fault with gouge zone approximately 10 mm thick. During the Sept. 21, 1999 Chi-Chi earthquake, the landslide mass slid from right to left along the bedding plane (yellow dashed line in Figure 2a) above the upper step. The gouge was soft and easily removed using metal tools.

sliding). Rotary-shear high-velocity friction experiments in the last two decades demonstrated that such dramatic slip-weakening indeed occurs for frictional sliding of rocks with or without fault gouge (e.g., Shimamoto and Tsutsumi, 1994; Tsutsumi and Shimamoto, 1996, 1997; Hirose and Shimamoto, 2005; Di Toro et al., 2006, 2011; Han et al., 2007; Mizoguchi et al., 2007), and for landslide materials too (Miyamoto et al., 2009; Yano et al., 2009; Ferri et al., 2010, 2011; Liao et al., 2011). Friction coefficient reduced to the order of 0.05 to 0.2 at seismic slip rates on the order of 1 m/s, allowing high speed landslide motion possible. Dong et al. (2013) conducted the Newmark analysis and successfully reproduced the Tsaoling landslide using a velocity- and displacement-dependent friction law to describe the results from high-velocity experiments on the Tsaoling landslide materials by Miyamoto et al. (2009). We employed the same approach in the study to refine further the analysis of the Tsaoling landslide motion, (1) by conducting high-velocity friction experiments on the gouge from bedding-parallel faults in the Cholan Formation close to the sliding surface during the Tsaoling landslide, (2) by compiling all existing data on the frictional properties of the Tsaoling landslide materials, and (3) by slightly modifying the velocity- and displacement-dependent friction law in the Newmark analysis of the landslide. We used a rotary-shear low- to high-velocity friction apparatus at the National Central University of Taiwan (LHVR-Taiwan) to study frictional behaviors of the fault gouge. The Tsaoling landslide mass was simplified as a rigid block (centroid of the moving block) and we idealized the landslide motion as the three stages of mass movement from the initiation to stop.

Recently, Togo et al. (2014) performed oscillatory velocity experiments on dry and wet shale gouge from the Tsaoling landslide site, by idealizing the Tsaoling landslide motion during the Chi-Chi earthquake as repeated accelerating/decelerating motion with a frequency ranging from 0.3 to 1.2 Hz. They observed small weakening and strengthening in association of the accelerating/decelerating motion, while undergoing overall slip-weakening. They successfully reproduced the Tsaoling landslide motion by the Newmark analysis with a simple exponential slip-weakening law. We use in this paper a more involved friction law, particularly by including the velocity dependence of the steady-state

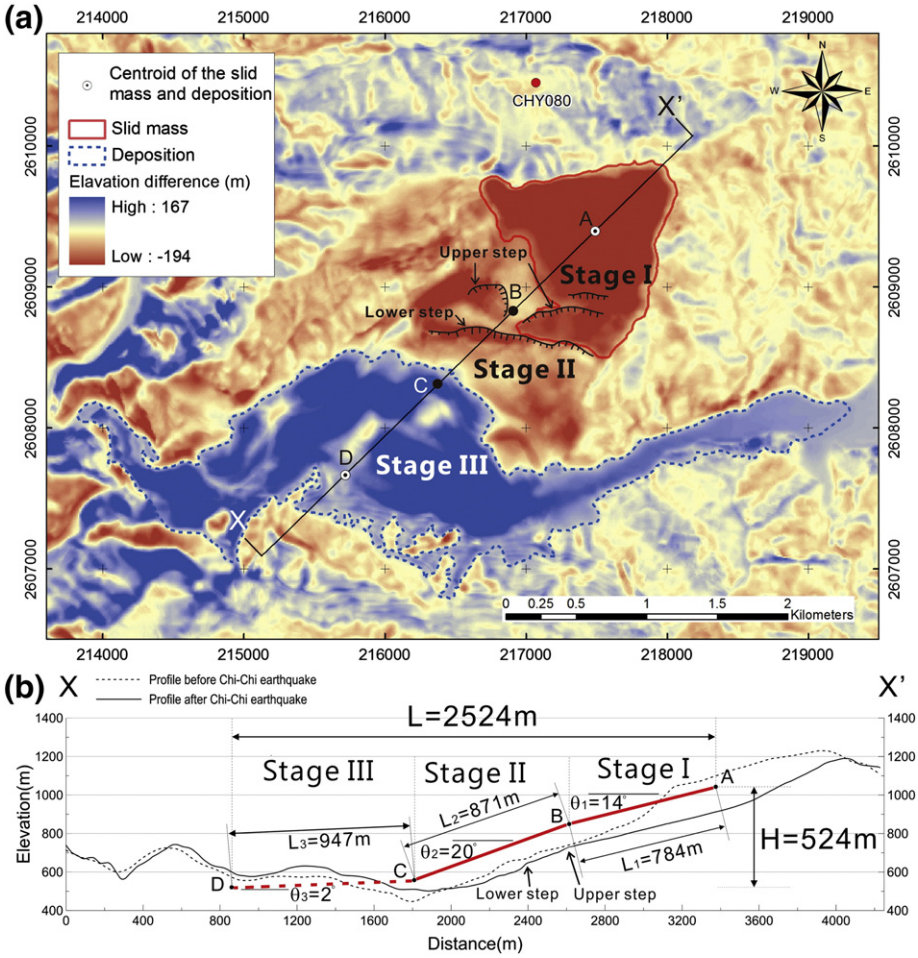


**Fig. 3.** (a) A color contour map of the Tsaoling landslide site showing the differences in elevation before and after the landslide, derived from pre- and post-event DTMs. The warm and cool colors indicate areas of erosion and deposition, respectively. Stages I to III and the related boundary points are marked in the figure. (b) Profile XX′ with the dashed and solid lines showing the ground surfaces before and after the Chi-Chi earthquake (Tsaoling landslide). The red solid and dashed lines represent the trajectory of the moving mass in Stages I to III, using the centroids of the landslide mass that were determined from the DTMs.

friction which can affect the high-velocity sliding portion of the Tsaoling landslide. We also compiled all existing friction data, including those by Togo et al. (2014). After our initial manuscript was submitted, an interesting paper was published by Chen et al. (2014) who conducted the Newmark analysis of the Tsaoling landslide by combining the results from traditional direct shear tests cited above and from high-velocity friction experiments by Miyamoto et al. (2009). Their results are similar to ours for the high-speed sliding part because they used a very low steady-state friction coefficient (0.05) after Miyamoto et al. (2009). They called it "mobilized friction angle" and distinguished it from the residual friction angle which is derived from the direct shear tests, and assumed arbitrarily that the friction drops instantly from the peak to residual friction, and then friction drops abruptly to mobilized friction at a displacement of 0.5 m. Those assumptions on the changes in friction are oversimplified and Newmark analysis of the triggering portion should be testified with real experimental results.

## 2. 1999 Tsaoling landslide event

### 2.1. Geological background

The Tsaoling landslide is located in central-western Taiwan in the Western Foothills geologic province (Figure 1). The Pliocene Chinshui Shale and the Cholan Formation crop out in the Tsaoling area. The Cholan Formation is more than 1000 m thick and consists of intercalated fine-grained sandstone and shale, whereas the Chinshui Shale consists of massive mudstone and shale having an average thickness of approximately 110 m. The Tsaoling anticline and the Chiusiungping syncline dominate the attitudes of the bedding planes at the landslide site, which have a dip direction and dip angle of 220–230° and 12–15°, respectively (Kuo et al., 2009; Tang et al., 2009; Lee, 2011). Four historical rock slides have occurred on the southwest slope of Mount Tsaoling between 1862 and 1979 (Hung et al., 2002); the landslides in 1862 and 1941 were triggered by earthquakes, and those in 1942 and 1979 were triggered by heavy rainfall. In addition, a large rock slide with a volume of 125-million $m^3$ and an average thickness of 140 m slid down Mount Tsaoling during the Sept. 21, 1999 Chi-Chi earthquake.

The Tsaoling landslide is a typical dip-slope rock slide that moved along bedding surfaces (Figure 2a). The Chingshui River cuts into the toe of the dip-slope and eliminates obstacles that would prevent landslide motion. The colluvium of the Tsaoling landslide was deposited on the other (SW) side of the Chingshui River and on Mount Daogiaoshan (Figure 2b). Flexural-slip along bedding shears commonly occur in alternating beds of folded sedimentary rocks (Donath and Parker, 1964; Tanner, 1989, 1992). Bedding-parallel shears or faults that develop in moderate to tight folds or fault-propagation folds, which can facilitate dip slope failures (Hart, 2000; Lee, 2012). Immediately below the exposed sliding surface in the Tsaoling area, we observed four bedding-parallel faults with outcrop lengths greater than 20 m that were spaced approximately 1 m apart (Figure 2c). We sampled gouge from the fault zones for high-velocity friction experiments (Figure 2d) at the site marked in Fig. 1. X-ray diffraction analysis revealed that the bedding-

parallel fault gouge contains quartz, plagioclase, illite, kaolinite, chlorite, and montmorillonite (Miyamoto et al., 2009). The liquid limit and plastic limit of the fault gouges are 23% and 6%, respectively. The fault gouge materials can thus be categorized as low-plasticity clays (CL) according to the Unified Soil Classification System.

### 2.2. Topography and motion of the Tsaoling landslide

Based on the post-event topography, two steps are present (Figure 1; upper and lower steps) in the landslide source area, and the three outcropping planar sliding surfaces parallel to the bedding plane in alternating beds (Chigira et al., 2003). Fig. 2a shows the upper step and the main sliding surface (yellow line). The main sliding surface is located within the Cholan Formation, but the lower part extends into the Chinshui Shale (Chen et al., 2014). Approximately 20% of the slide mass dropped into the Chingshui River, which created a 5-km-long landslide dam and reservoir. The landslide deposit included rock blocks greater than 10 m in diameter. A village with 39 residents and visitors slid with the landslide mass, and some of the houses were moved to the top of Mount Daogiaoshan without being buried in debris (cf. Chen et al., 2004, 2014). Surprisingly, 7 people survived the catastrophic landslide.

We determined the centroids of the sliding mass (Point A) and landslide deposit (Point D) in the following manner by determining the distribution of the elevation-difference using the pre- and post-event DTMs (Figure 3a). We made slices of landslide body and landslide deposits of 5 m in width using a GIS software and determined the mass distributions in the slices. Then the moment balance equations can be solved for the coordinates of the centroids as unknowns for accurate determinations of the centroids, plotted on a profile XX′ as points A and D. The horizontal and vertical displacements from A to D were 2524 m and 524 m, respectively, and the apparent friction angle is 0.21. The horizontal projection of the vector from Point A to Point D is almost identical to the sliding direction (dip direction, 226°). Fig. 3b shows profile XX′, which is located along the vector from A to D. Points B and C are the locations of the upper step and the Chingshui River Valley, respectively. The landslide process can be summarized as follows:

The initiation of movement of the mass (Point A) was triggered by the earthquake, and the mass slid in the dip direction of the bedding plane. The friction on the sliding plane controlled the mass movement. When the landslide mass passed through the upper (Point B) and lower steps (Figures 1 and 3), it "dropped" slightly and continued sliding along the bedding planes. The mass then "moved through" in the Chingshui River Valley (Point C) and finally hit Mount Daogiaoshan (Point D). A large amount of energy would have been dissipated by the collision and disintegration of the fast-moving mass. After the collision, the mass flowed up- and down-stream along the river bed. Accordingly, three stages of the Tsaoling landslide can be identified based on the aforementioned processes (Figure 3a and b). Stages I, II, and III are identified as the motions from A to B, B to C, and C to D, respectively.

In view of the kinematics of the Tsaoling landslide, we idealize the Tsaoling landslide as follows. (1) In Stage I (from A to B in Figure 3b), the landslide movement is idealized as a rigid-body sliding of the landslide mass along a flat bedding plane dipping 14°. (2) In Stage II (from B to C), the landslide mass went over two steps on surface topography (Figure 2a) as it entered into Stage II and must have fragmented to some degree, but we treat it as a rigid-block sliding along a steeper plane dipping 20°. (3)In Stage III (from C to D), the landslide block must have broken into fragments when it collided against the southwestern bank of the Chingshui River (Point C), and the surface topography is quite irregular from point C to the Mt. Daogiaoshan (Figures 2b and 3b). Thus a simple rigid-block motion along a planar surface is no longer applicable to the stopping phase of the landslide in Stage III, and this paper will not attempt to analyze the landslide behavior in Stage III. With those idealization of landslide motion in Stages I and II, frictional properties along the sliding surfaces are critical in conducting the landslide analysis. Thus, the next two sections will be devoted to the high-velocity frictional properties of the landslide materials.

## 3. Friction experiments on bedding-parallel fault gouge — low- to high-velocity rotary-shear tests

### 3.1. A low- to high-velocity rotary-shear friction apparatus

A high-velocity rotary-shear friction apparatus developed by Shimamoto and Tsutsumi (1994) and Hirose and Shimamoto (2005) has been widely used in friction experiments on fault rocks (e.g., Di Toro et al., 2011; references therein). The fifth author (TS) developed a second machine that expanded the capability of the apparatus to a wide range of velocities from 5 mm/yr to almost 10 m/s (see Togo and Shimamoto (2012) for the details of the second apparatus). In this study, we used a third-generation low- to high-velocity rotary-shear friction apparatus (Marui Co. Ltd, Osaka, Japan, MIS-233-1-78), that was designed by TS and installed at the National Central University of Taiwan in 2011 (Figure 4). The apparatus is capable of producing slip rates of 30 mm/yr to 1.3 m/s on 25-mm-diameter solid cylindrical specimens at normal stresses up to 20 MPa. A unique feature of the apparatus is a large chamber in which a variety of specimen assemblies, such as a hydrothermal pressure vessel, can be developed and mounted easily.

The apparatus consists of a 7.5 kW servomotor (1 in Figure 4a), a gear/belt system for low, intermediate and high velocities (2), a rotary encoder and potentiometer for monitoring the rotary motion (3), an upper rotary piston (4), a stationary lower piston (5), a cantilever-type torque gauge (6), an axial displacement transducer (7), an axial force gauge (8), and an air actuator (Fujikura Composites, Bellofram Cylinder) for applying axial loads up to 10 kN (9). The gear/belt system is composed of belts, gears, two gear boxes, and five electromagnetic clutches (Figure 4b) and can achieve a range of slip rates of almost 9 orders of magnitude by changing the motor speed (1.5–1500 rpm) and/or gear/belt lines. Five electromagnetic clutches allow velocity increases of $10^3$ or $10^6$ times by changing the gear/belt lines without stopping the motor. Torque is measured by a cantilever-type force gauge with an arm and two force gauges at both ends (Figure 4c). The normal stress on the sliding surfaces can be kept nearly constant even if the specimen shortens by controlling the air pressure in the Bellofram cylinder (Figure 4d) with a regulator. The axial force and axial displacements are measured with a strain-gauge-based force gauge and a displacement transducer, respectively (Figure 4a).

Hollow or solid cylindrical specimens with outer diameters of 25 mm are set between points 4 and 5 in Fig. 4a using an ETP bush from Miki Pulley Co. Ltd., Japan. This bush is a cylindrical flat-jack that can be tightened by turning a bolt with a torque wrench to hold a specimen tightly against the inner wall of the cylinder. The specimen has to be slightly less than 25 mm in diameter to prevent permanent deformation of the ETP bushes. A disadvantage of rotary shear apparatuses is the large gradient in slip rate across the sample from zero in the center to the maximum at the periphery. Because the shear velocity is not constant along the radius of the cylinder, an equivalent slip velocity ($V_{eq}$) is defined such that $V_{eq}S$ gives the rate of frictional work over a sliding surface with an area $S$, assuming a uniform shear stress (Shimamoto and Tsutsumi, 1994; Hirose and Shimamoto, 2005). For hollow cylindrical specimens with outer and inner diameters $r_1$ and $r_2$, respectively, $V_{eq}$ is given by:

$$V_{eq} = \frac{4\pi R\left(r_1^2 + r_1 r_2 + r_2^2\right)}{3(r_1 + r_2)} \tag{1}$$

where $R$ is the revolution rate of the motor. We used solid cylindrical specimens that were 25 mm in diameter ($r_1 = 0.0125$ m and $r_2 = 0$ m), and the maximum revolution rate of 1500 rpm gives a maximum equivalent slip rate of 1.3 m/s. Hereafter, the equivalent slip velocity is referred to simply as "velocity" or "slip rate" $V$.

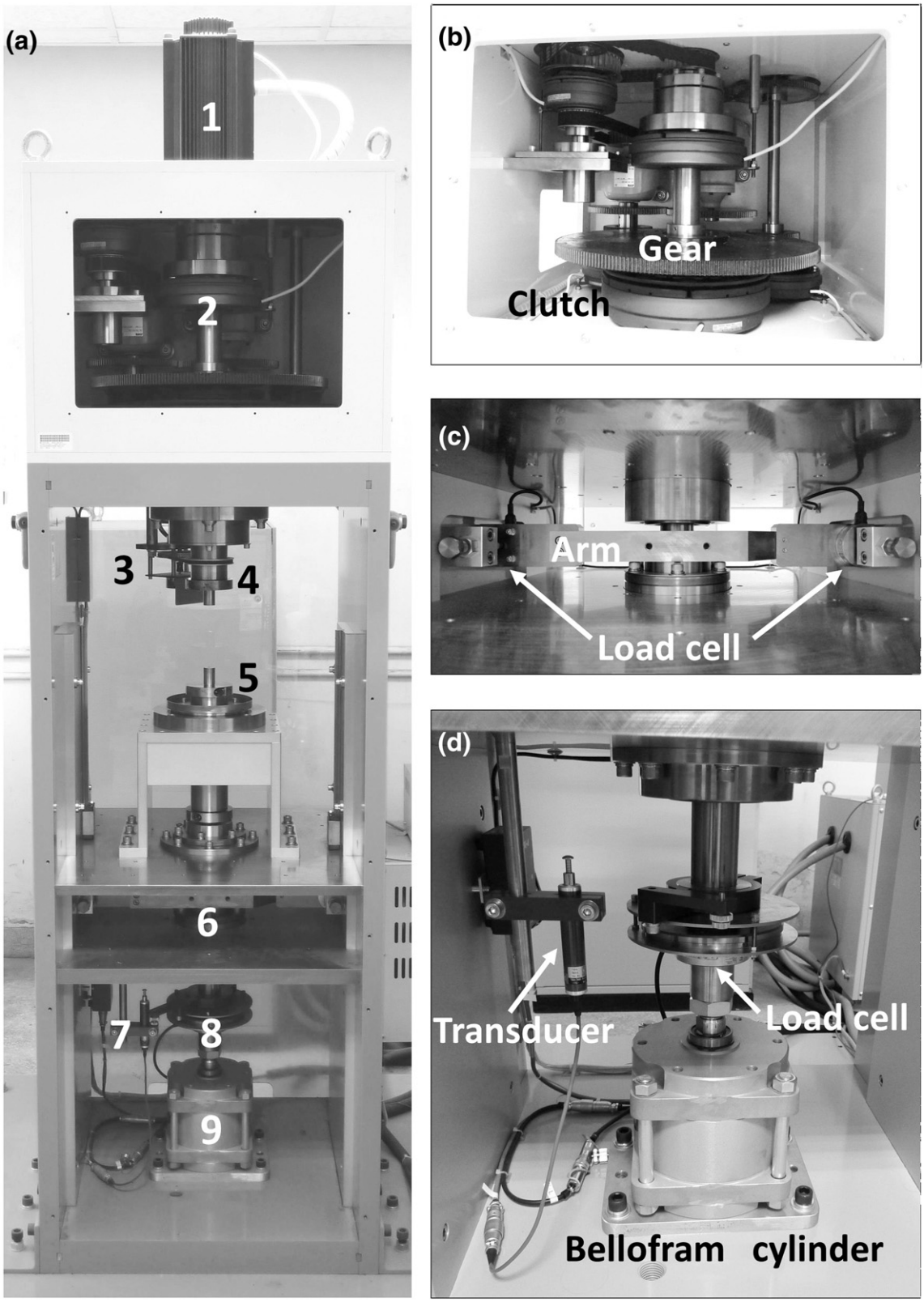


**Fig. 4.** Photographs showing (a) the rotary-shear low- to high-velocity frictional testing apparatus at the National Central University of Taiwan (LHVR-Taiwan, built by Marui Co. Ltd., Osaka, Japan), (b) the gear/belt system for three ranges of velocities, (c) the cantilever-type torque gauge, and (d) the bottom part with a Bellofram cylinder, an axial load cell, and an axial displacement transducer. The part numbers in (a) are used in the description of the apparatus in the text.

### *3.2. Experimental procedures*

Friction experiments were conducted on fault gouge collected from near the sliding surface of the Tsaoling landslide under a normal stress ($\sigma_n$) of 3 MPa, at slip rates of 0.0023 to 1.30 m/s and with displacements up to 53 m. The normal stress corresponds to the overburden pressure of the 140-m-thick sliding mass and the density of rock is 2430 kg/m$^3$ (Hung, 1982). The tests were performed at room temperature and

room humidity conditions. We conducted the friction experiments on the fault gouge following the procedures of Mizoguchi et al. (2007). The fault gouges were sandwiched by a pair of solid cylinder of gabbro samples that were 25 mm in diameter and surrounded by a Teflon sleeve (Figure 5). The inner diameter of the Teflon sleeve was approximately 100 μm smaller than the specimen diameter to impose a pressure on the specimen and prevent the loss of fault gouge (see Appendix of Sawai et al. (2012) for a description of problems caused by Teflon sleeves). The sliding surfaces of the specimens were roughened by grinding them with #80 silicon carbide abrasive (180 μm in size) so the fault gouge would deform rather than slipping at the gouge-rock interfaces. The specimen alignment was adjusted to within several microns to avoid distortion of the Teflon sleeve that would lead to fault gouge leakage and erratic frictional behavior. Gouge particles smaller than 150 μm were selected using a #100 sieve to avoid mixing of large particles in the approximately 1-mm-thick gouge zone (1 g of gouge). Distilled water was added to the samples to keep the water content ($w$) nearly identical to the natural water content of the fault gouge (~25%). The details of preparing the samples can be found in Togo et al. (2011). After the gabbro specimens with fault gouge were placed in the apparatus, the axial stress was increased to 3 MPa within approximately 1 min, and the specimens were left at this normal stress until the axial displacement due to gouge compaction had stopped. It usually took approximately 10–15 min to fully consolidate the gouges, and some water was squeezed out during consolidation; i.e., the water content in the gouges during the experiments was less than 25%.

### 3.3. Experimental results on bedding-parallel fault gouge

The results from the friction experiments on the gouge from the bedding-parallel faults at a slip rate $V$ of 0.0023 to 1.3 m/s reveal three types of frictional behavior: (1) slip-strengthening behavior to the peak friction followed by slight slip-weakening or nearly constant friction (Figure 6a; $V = 0.0023, 0.0124, 0.0436$, and 0.1 m/s); (2) transitional behavior with slip-strengthening to the peak friction followed by slip-weakening (Figure 6b; 0.22 m/s); and (3) marked slip-weakening behavior (Figure 6c to f; $V = 0.43, 0.50, 0.87$, and 1.30 m/s). The slip-strengthening behavior at low slip rates is similar to the results from traditional direct shear tests of normally consolidated clay. The ultimate friction coefficients $\mu_{ult}$, defined as the friction coefficient as the shear displacement approaches infinity, were within a narrow range of 0.4–0.5 (Figure 6a). We calculated $\mu_{ult}$ by taking an average of the measured friction coefficients at shear displacements of greater than 2 m (Table 1). The value of $\mu_{ult}$ increases with decreasing slip rate; this could be due to the loss of water from the gouge in the slow experiments. At shear velocities greater than 0.43 m/s, the peak friction was reached very quickly and was followed by marked slip-weakening (Figure 6c–f). The post-peak slip-weakening can be described by an empirical slip-weakening law after Mizoguchi et al. (2007):

$$\mu(d) = \mu_{ss} + \left(\mu_p - \mu_{ss}\right) \exp(\ln(0.05) d/D_c) \tag{2}$$

where $\mu(d)$ is the friction coefficient at a displacement $d$, $\mu_p$, and $\mu_{ss}$ are the peak and steady-state friction coefficients (friction coefficient when the displacement approach to infinity), respectively, and the slip-weakening distance $D_c$ is defined as the displacement at which $\mu$ decreases by 95% ($\mu_p^- \mu_{ss}$). This definition can be confirmed by substitution of $d = D_c$ into Eq. (2), which yields $(\mu(D_c)^- \mu_{ss}) = 0.05\ (\mu_p^- \mu_{ss})$ (see Figure 7 and the dashed lines in Figure 6c–f). The slip-weakening parameters $\mu_p$, $\mu_{ss}$, and $D_c$ are listed in Table 1.

The behavior at $V = 0.22$ m/s is transitional between the slip-strengthening and the slip-weakening behaviors; i.e., the peak friction was reached at $d = 1$–2 m and it is followed by minor slip-weakening (Figure 6b). For the transitional behaviors, we read $\mu_p$ directly from the curves and determined $\mu_{ss}$ by taking an average of the measured values of $\mu$ for $d > 2$ m for LHVR0122 and $d > 4$ m for LHVR0252, 0257, and 0259 (see Table 1 for the values). The water contents of the samples generally decreased from 25% to 18% after consolidation.

The derived ultimate and peak friction coefficients are compared with those that were obtained from direct shear tests. First, we compiled three documented strength datasets of shale samples from the Tsaoling landslide site, using traditional direct shear test at slip rates of $10^{-6}$ to $10^{-5}$ m/s (WRA, 2000; Lee, 2001; Towhata et al., 2001), and compared with our experimental results (Figure 8). The peak friction coefficient of the tested shale with its natural water content ($w = 2.2$–5.6% after the direct shear test) was approximately 0.8 (Lee, 2001). The residual friction coefficients ranged from 0.3 to 0.6 (WRA, 2000; Lee, 2001; Towhata et al., 2001) and had an average value of 0.43 (Figure 8). It is notable that the lowest residual friction coefficient of approximately 0.3 was obtained for a slickensided discontinuity in a shale sample.

In the slip-strengthening regime (velocities from 0.001 to 0.1 m/s), the average ultimate friction coefficient ($\mu_{ult}$; blue circles) of the tested wet fault gouges is 0.44 (Table 1 and Figure 8), which is nearly identical to the friction coefficient obtained from traditional direct shear tests of wet shale (0.43). In the transitional and slip-weakening regimes (velocity > 0.1 m/s), the average peak friction coefficient ($\mu_p$; hollow circles) is 0.38 (Table 1 and Figure 8), which is slightly less than the ultimate value in the slip strengthening regime. As mentioned previously, the friction coefficient decreased from a peak value to a steady-state value with increasing displacement in the slip-weakening regime. The steady-state friction coefficients ($\mu_{ss}$; red circles with crosses) decreased from approximately 0.27 to 0.05 with increasing velocity (Figure 8), which has been observed in numerous studies of high-velocity rotary shear tests (Miyamoto et al., 2009; Togo et al., 2014). The slip-weakening distances ($D_c$) for our data range from 2.94 to 8.55 m with an average value of 4.90 m (Table 1).

Previous studies (e.g., Togo et al., 2011) proposed a velocity dependent steady-state friction coefficient that can be expressed by:

$$\mu_{ss}(V) = \mu_{ss}^{\infty} + \left(\mu_p - \mu_{ss}^{\infty}\right) \exp\left(\frac{-V}{V_c}\right) \tag{3}$$

where the friction coefficient $\mu_{ss}^{\infty}$ is defined as the steady-state friction coefficient when the shear velocity approaches infinity and $V_c$ is a

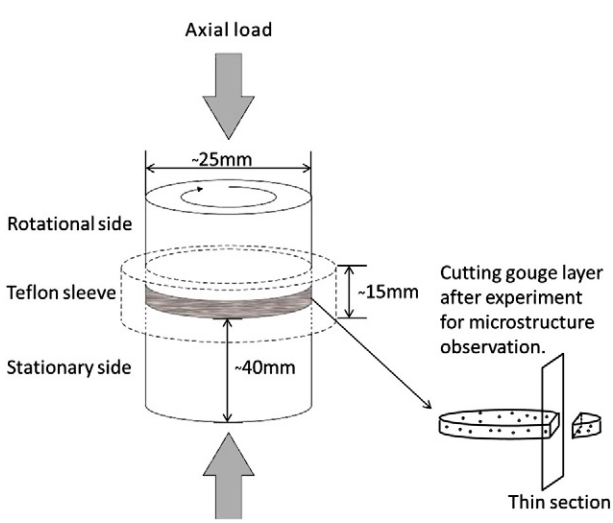


**Fig. 5.** Schematic of the sample assembly used in the friction experiments. Thin sections of the deformed fault gouge were prepared for microstructural observations along a surface shown in the lower-right corner.

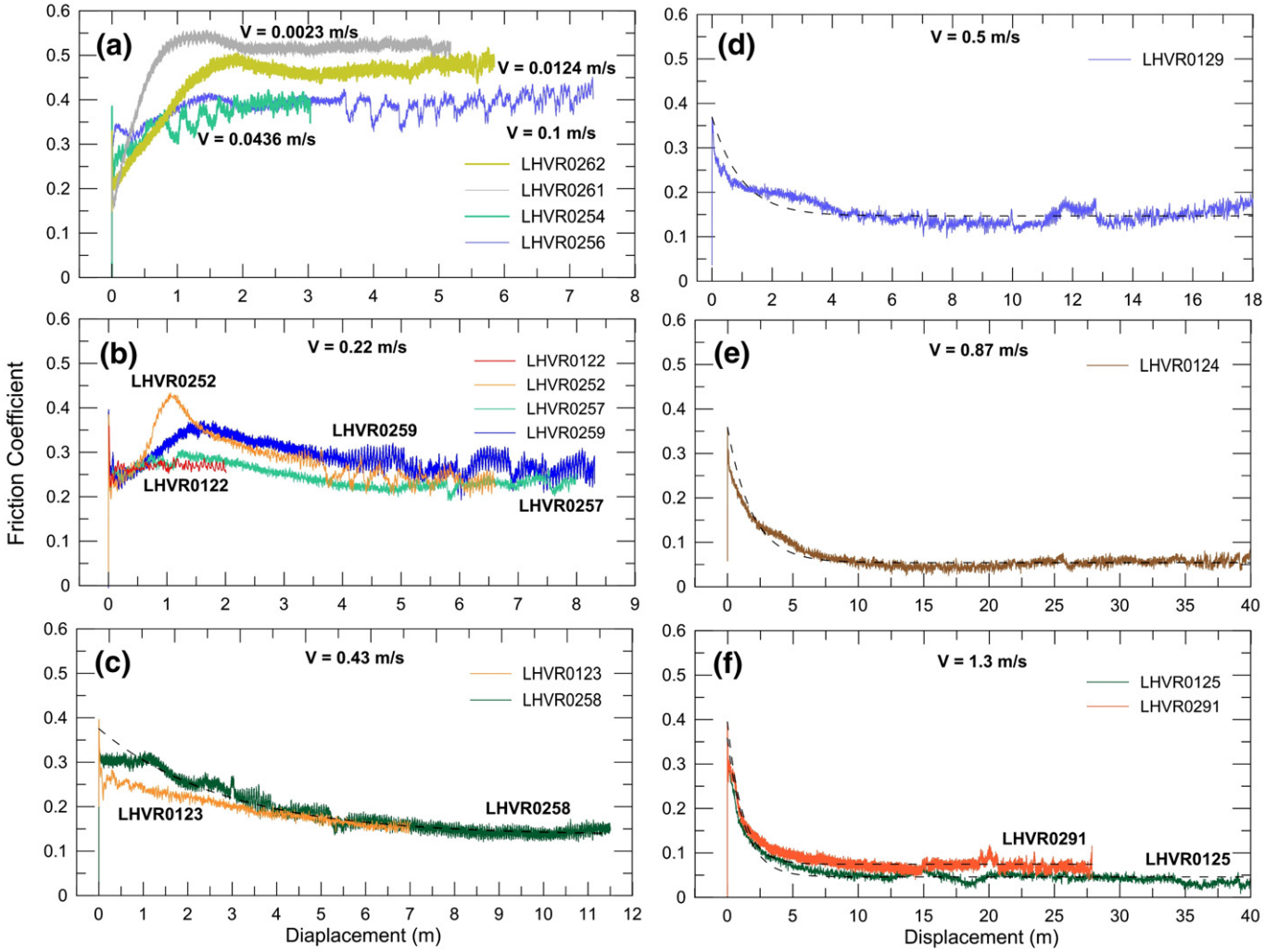


**Fig. 6.** Curves of friction coefficient versus shear displacement for fault gouges from a bedding-parallel fault near the sliding surface of the Tsaoling landslide showing (a) slip-strengthening behavior, (b) transitional behavior, and (c) to (f) slip-weakening behavior. The shear velocities are given in the diagrams. The dashed lines show the least-squares fits to the experimental data using an empirical slip-weakening law (Eq. (2)).

material constant. This equation was proposed to describe a change in $\mu_{ss}$ only in the slip-weakening regime, so that we modified the equation to describe $\mu_{ss}$ in both slip-weakening and strengthening regimes as follows. The frictional coefficient in the slip-strengthening regime was assumed to be a constant ($=\mu_{ult}$) when the shear velocity is less than a critical velocity $V_{critical}$ and $\mu_{ss}$ was described by a similar equation as in Eq. (2) for velocity greater than $V_{critical}$.Then the changes in friction coefficients are shown by thick solid curves in Fig. 8 and given by:

$$\begin{aligned} &\mu(V) = \mu_{ult} = 0.44 && \text{for } V < V_{critical} \\ &\mu_{ss}(V) = \mu_{ss}^{\infty} + \left(\mu_p - \mu_{ss}^{\infty}\right)\exp[-(V - V_{critical})/V_{critical}] && \text{for } V \geq V_{critical} \\ &\mu_p = 0.38 && \text{for } V \geq V_{critical} \end{aligned} \tag{4}$$

**Table 1**
Experimental conditions and slip-weakening parameters in Eq. (2) for the bedding-parallel fault gouge.

| | Slip velocity [m/s] | $\sigma_n$ [MPa] | Test numbers | $\mu_{ult}$ | $\mu_p$ | $\mu_{ss}$ | $D_c$[m] |
|---|---|---|---|---|---|---|---|
| Slip-strengthening regime | 0.0023 | 3 | LHVR0261 | 0.52 | – | – | – |
| | 0.0436 | 3 | LHVR0254 | 0.47 | – | – | – |
| | 0.0124 | 3 | LHVR0262 | 0.39 | – | – | – |
| | 0.10 | 3 | LHVR0256 | 0.39 | – | – | – |
| Mean value | | | | 0.44 | | | |
| Transition regime | 0.22 | 3 | LHVR0122 | – | 0.36 | 0.27 | – |
| | 0.22 | 3 | LHVR0252 | – | 0.38 | 0.24 | – |
| | 0.22 | 3 | LHVR0257 | – | 0.38 | 0.23 | – |
| | 0.22 | 3 | LHVR0259 | – | 0.40 | 0.27 | – |
| Slip-weakening regime | 0.43 | 3 | LHVR0123 | – | 0.40 | 0.18 | |
| | 0.43 | 3 | LHVR0258 | | 0.36 | 0.13 | 8.55 |
| | 0.50 | 3 | LHVR0129 | – | 0.37 | 0.15 | 2.94 |
| | 0.87 | 3 | LHVR0124 | – | 0.36 | 0.05 | 5.60 |
| | 1.30 | 3 | LHVR0125 | – | 0.36 | 0.05 | 3.97 |
| | 1.30 | 3 | LHVR0291 | – | 0.40 | 0.08 | 3.42 |
| Mean value | | | | | 0.38 | | 4.90 |

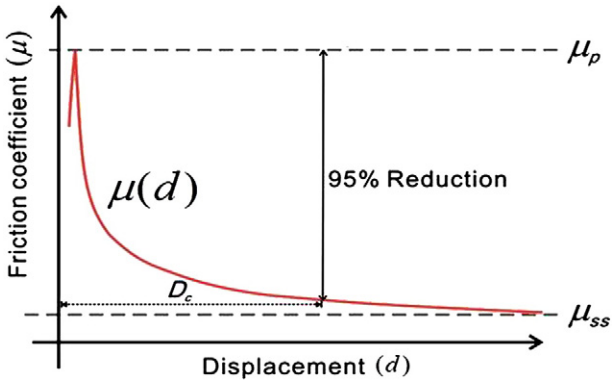


**Fig. 7.** Schematic diagram showing a slip-weakening behavior described by an empirical law (Eq. (2)).

where $\mu_p$ is the peak friction coefficient in the slip-weakening regime. In this study, Eqs. (2) and (4) were used to calculate the velocity–displacement dependent friction coefficient for the Newmark analysis. The calibrated parameters are as follows: $\mu_{ult} = 0.44$, $\mu_p = 0.38$, $\mu_{ss}^{\infty} = 0.076$, $D_c = 4.9$ m (an average of $D_c$ in Table 1), and $V_{critical} = 0.15$ m/s (cf. black curve in Figure 8).

### 3.4. Microstructural observations

Microstructural observations were made on thin sections of the deformed fault gouge samples impregnated with epoxy. The samples were cut parallel to the specimen axis between the center and margin of the specimens (Figure 5). A field emission environmental SEM (JEOL JSM-7000 F) with an accelerating voltage of 15 or 20 kV was utilized to observe the microstructures. Back-scattered electron images (BSIs) of carbon-coated thin sections are shown in Figs. 9–13. The top of the BSIs are the rotational sides, and the arrows indicate the shear sense. The black areas represent the epoxy used to glue the sample.

The microstructures of the tested fault gouge in the slip-weakening regime are illustrated first. Fault gouge samples LHVR0125 and 124, in which the slip rates were 0.87 and 1.30 m/s, respectively, were slipped 40 m and 53 m, respectively. Highly deformed zones with ultrafine grains (the "U" layer) were observed near the rotational sides (Figures 9 and 10). The U layers consisted of ultrafine grains that were mostly less than 1 μm in diameter and appeared to be welded or sintered. Similar textures were reported previously (Sawai et al., 2012; Togo and Shimamoto, 2012; Yao et al., 2013a, 2013b). These highly deformed zones consisting of ultrafine grains may be slip zones in which the shear deformation was concentrated. Clast-clay aggregates (CCAs) are commonly observed within the moderately deformed zones below the "U" layers. The moderately deformed zones and CCAs are shown in Fig. 9c and d and Fig. 10c and d. Similar to microstructures, the presence of the U layer and moderately deformed zones with CCAs can be observed in the fault gouge after a slip distance of approximately 18 m at a velocity of 0.5 m/s (LHVR 0129; Figure 11). Two U layers are shown in Fig. 11b, and detailed photomicrographs are shown in Fig. 11c and d.

The transitional and slip-strengthening regimes are described below. Fig. 12 shows BSIs of sample LHVR0259 (slip velocity of 0.22 m/s), and Fig. 12b–d shows the highly deformed zones, including the U layer. The U layer is well-developed, as was observed in the samples from the slip-weakening regime. Continuous U layers are absent when the shear velocity was less than 0.22 m/s (slip-strengthening regime). The U layer can be observed at a slip velocity of 0.1 m/s (Figure 13a) but is less extensive (only approximately 4 mm wide). The fault gouges from the low slip velocity tests (LHVR0261, 262, 254; slip rates of 0.0023–0.0436 m/s) having total slip of 3.0–7.4 m show uniform deformation textures with few low angle fractures (Figure 13b and c) or no observable fractures (Figure 13d). Interestingly, CCAs are absent in the transitional and slip-strengthening regimes.

## 4. Compilation of existing friction data from the Tsaoling landslide materials

### 4.1. Friction behaviors of shale powder and fault gouge under dry and wet conditions

Two datasets of rotary shear tests using dry and wet samples from the Tsaoling landslide site have been reported (Miyamoto et al., 2009; Togo et al., 2014). Togo et al. (2014) documented the friction coefficients of dry shale powders of samples from the lower Cholan Formation near the slide plane (squares in Figure 14), and Miyamoto et al. (2009) reported friction coefficients of dry bedding-parallel fault gouges (triangles in Figure 14). In the slip-strengthening regime (velocities from 0.001 to 0.1 m/s), the ultimate friction coefficient ($\mu_{ult}$; squares with crosses) of the tested dry shale powder is higher than those of the wet fault gouges obtained in this study (solid blue lines) and those from traditional direct shear tests of wet shale. In the

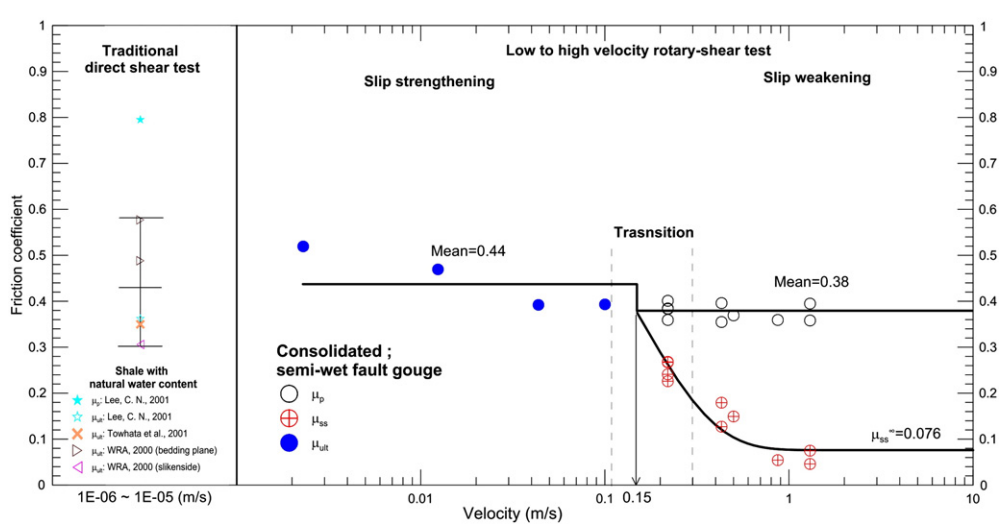


**Fig. 8.** Friction coefficients of the tested bedding-parallel fault gouge collected from the Tsaoling landslide site and fitting with our idealized velocity–displacement friction law (black lines). $\mu_{ult}$ is the friction coefficient at velocities less than $V_{critical}$ (=0.15 m/s), $\mu_p$ and $\mu_{ss}$ are the peak and steady-state friction coefficient in the slip-weakening regime, respectively. The left part shows the results of traditional direct shear tests (WRA, 2000; Lee, 2001; Towhata et al., 2001).

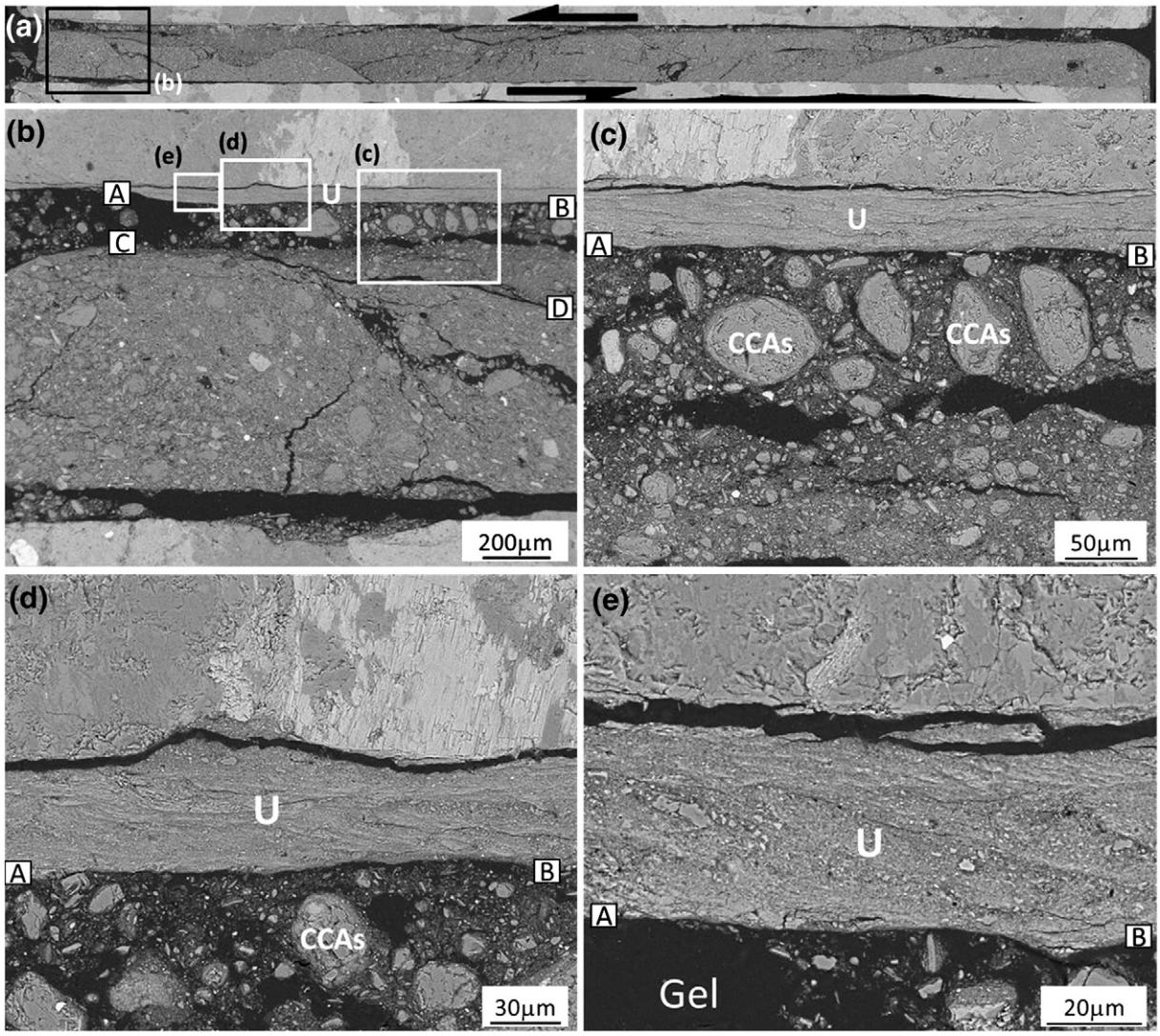


**Fig. 9.** Back-scattered electron images of fault gouge deformed at a normal stress of 3 MPa and a slip rate of 1.3 m/s (LHVR0125). (a) Photomicrograph showing the textures of the deformed fault gouge. (b) a close-up photomicrographs of the rectangular frame in (a), and (c), (d) and (e) are close-up photomicrographs of rectangular portions with corresponding marks in (b). The U layer and CCA layer are above and below AB, respectively. Although CD is a sharp surface, CCAs are present above and below CD. It mainly comprised of foliated mineral with few quartz grains.

transition and slip-weakening regimes (velocity > 0.1 m/s), the peak friction coefficients ($\mu_p$) of dry shale powders (solid squares) and dry fault gouges (solid triangles) are nearly the same as the ultimate friction coefficients in the slip-strengthening regime. These values ranged from approximately 0.6 to 0.8 with a mean value of 0.7, which is similar to the typical Byerlee (1978) friction values that range from 0.6 to 0.85. Notably, these ultimate and peak values are much higher than those of the wet fault gouges (approximately 0.4 to 0.5) obtained in this study.

As mentioned previously, the friction coefficient decreased from the peak to a steady-state value with increasing displacement in the slip-weakening regime. The steady-state friction coefficients ($\mu_{ss}$) of dry shale powders and dry fault gouges (hollow squares and triangles) decreased from approximately 0.5 to 0.1 with increasing velocity. As expected, the steady-state friction coefficients of the dry samples are higher than those of the wet fault gouges obtained in this study (approximately 0.27 to 0.05).

In addition to dry samples, Miyamoto et al. (2009) documented a dataset of friction coefficients in the weakening regime using wet shale powders and fault gouges sampled from the Tsaoling landslide site. The friction behaviors of the wet shale powders and wet fault gouges reported by Miyamoto et al. (2009) are shown in Fig. 15. The peak friction coefficients of the wet shale powders (average value of 0.61) are similar to those of dry powders reported by Togo et al. (2014) (Figure 14) while the steady-state values are similar with those of wet fault gouges derived from this study (solid gray lines).

The reported values of $\mu_{ss}$ of the wet fault gouges are also similar to our experimental results (Figure 15). The average $\mu_p$ of the wet fault gouges (0.22) is the lowest of all of the datasets. Notably, although the fault gouge samples are identical to those in this study, the consolidation procedure was not adopted by Miyamoto et al. (2009). Therefore, the initial water contents of the fault gouge samples tested in this study are less than those used in Miyamoto et al. (2009). The excess pore pressure generated by the normal load is inferred to have dissipated during the consolidation procedure and resulted in higher peak strengths obtained in this study. The microstructures of the sheared samples with different water contents will be compared in Section 6.3. To discriminate the wet fault gouges, the term “semi-wet fault gouge” is used in the following discussion to represent the samples from this study, and “wet fault gouge” is used for the samples of Miyamoto et al. (2009). The influence of the frictional behaviors at different water contents on the initiation and kinematics of the earthquake-triggered landslide will be elucidated further in Section 5.3.

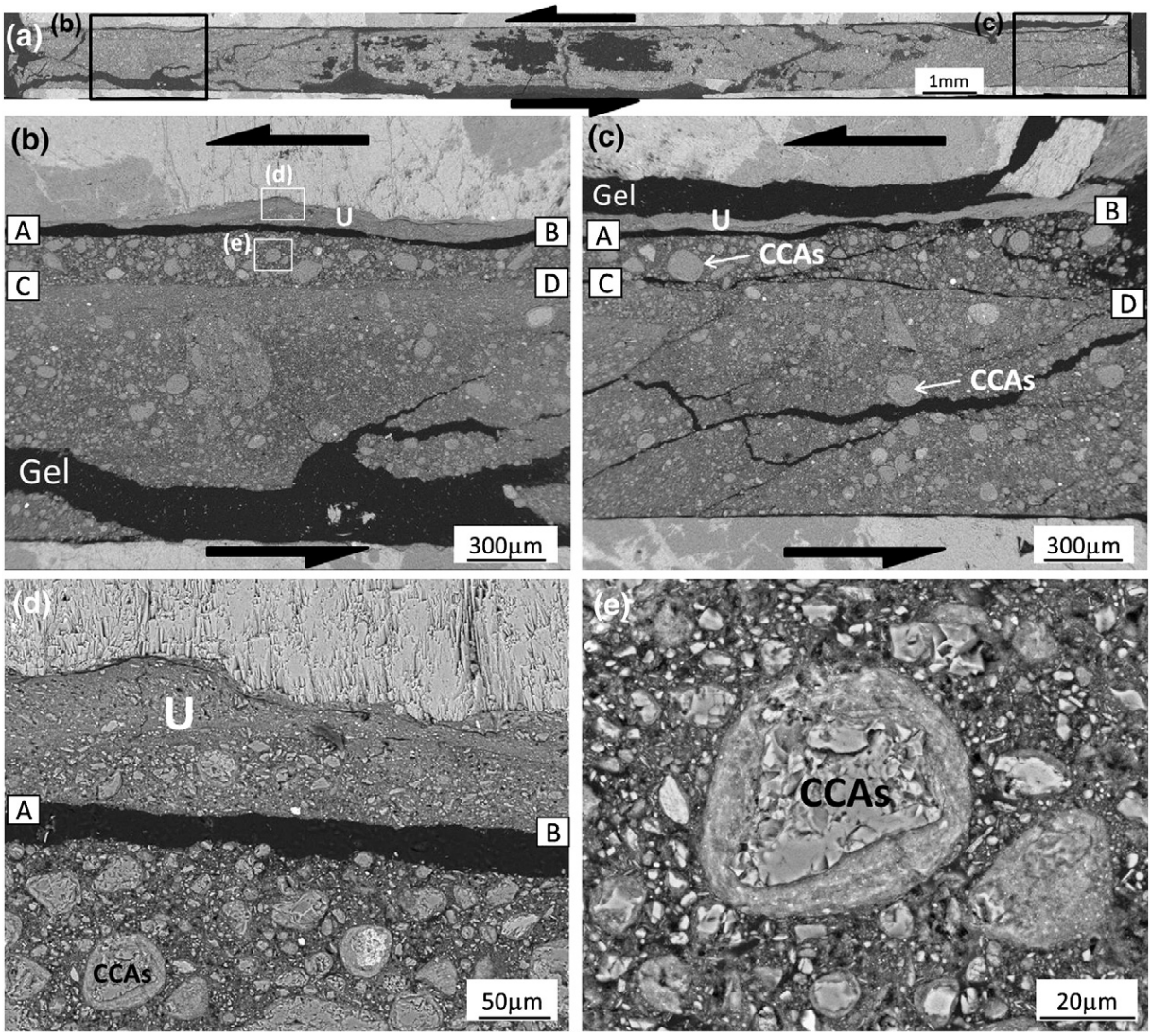


**Fig. 10.** Back-scattered electron images of fault gouge deformed at a normal stress of 3 MPa and a slip rate of 0.87 m/s (LHVR0124). (a) Photomicrograph showing the textures of the deformed fault gouge. (b and c) Detailed photomicrographs of the stratified fault gouge zone. The U layer and CCA layer are above and below AB, respectively. Although CD is a sharp surface, CCAs are present above and below CD. (d) Detailed photomicrograph of the U layer. (e) Detailed photomicrograph of CCAs between AB and CD. The thickness of the cortex of this CCA is approximately 10 μm.

### *4.2. Velocity-dependence of the slip-weakening parameters*

To evaluate the effect of the water content on the kinematics of the Tsaoling landslide, the parameters of the proposed friction law for all of the published datasets were calibrated. For simplicity, the ultimate and peak friction coefficients are assumed to be identical. The peak friction coefficients $\mu_p$ of the dry shale powder (Togo et al., 2014), wet shale powder, and wet fault gouge (Miyamoto et al., 2009) are 0.70, 0.61, and 0.22, respectively. Accordingly, $\mu_{ss}^{\infty}$ and $V_{Critical}$ in Eq. (4) of all of the datasets can be calibrated using the least-squares curve fitting technique. The velocity dependent steady-state friction coefficients that incorporate the calibrated parameters of all of the datasets are shown in Fig. 16a and the calibrated parameters are listed in Table 2. In general, the steady-state friction coefficients of the dry materials are slightly higher than those of the wet materials. The $\mu_{ss}^{\infty}$ value of the dry materials is 0.162, which is higher than that of the wet material (0.076–0.098). The critical velocities ($V_{Critical}$) that separate the slip-weakening and slip-strengthening regimes are within a narrow range (0.1–0.15 m/s) for different water contents.

Togo et al. (2014) reported the $D_c$ values of the tested materials for different velocities. The $D_c$ values of the tested samples of Miyamoto et al. (2009) were calibrated using the reported experimental results. Fig. 16b shows the slip-weakening distance ($D_c$) of all of the dry and wet samples from the Tsaoling landslide site. The values of $D_c$ range from 1 to 9 m with the exception of the wet fault gouges reported by Miyamoto et al. (2009). The documented $D_c$ values of the dry samples (fault gouges and shale powders) and wet shale powder decrease with increasing shear velocity. Togo et al. (2011) and Yao et al. (2013a) fit the dependence of $D_c$ on the slip rate and the normal stress as a power law. We use their empirical equation in a form:

$$D_c(V) = a(V/V_0)^{-b} \tag{5}$$

where $a$ and $b$ are constants ($a$ has a dimension [length], and $b$ is dimensionless), and $V_0$ was introduced for the dimensional consistency (we take $V_0 = 1$ m/s in this study). The values of $a$ and $b$ of the dry samples (shale powders and fault gouges) and wet shale powder were calibrated and the fit line (Eq. (5)) are shown in Fig. 16b (red and blue lines). In addition, the black dashed line represents the fitted curve of all of the data (dry and wet samples). The calibrated parameters are listed in Table 3. The trend of the velocity dependency on the slip-weakening distance is not clear for the wet fault gouges. The extremely low slip-

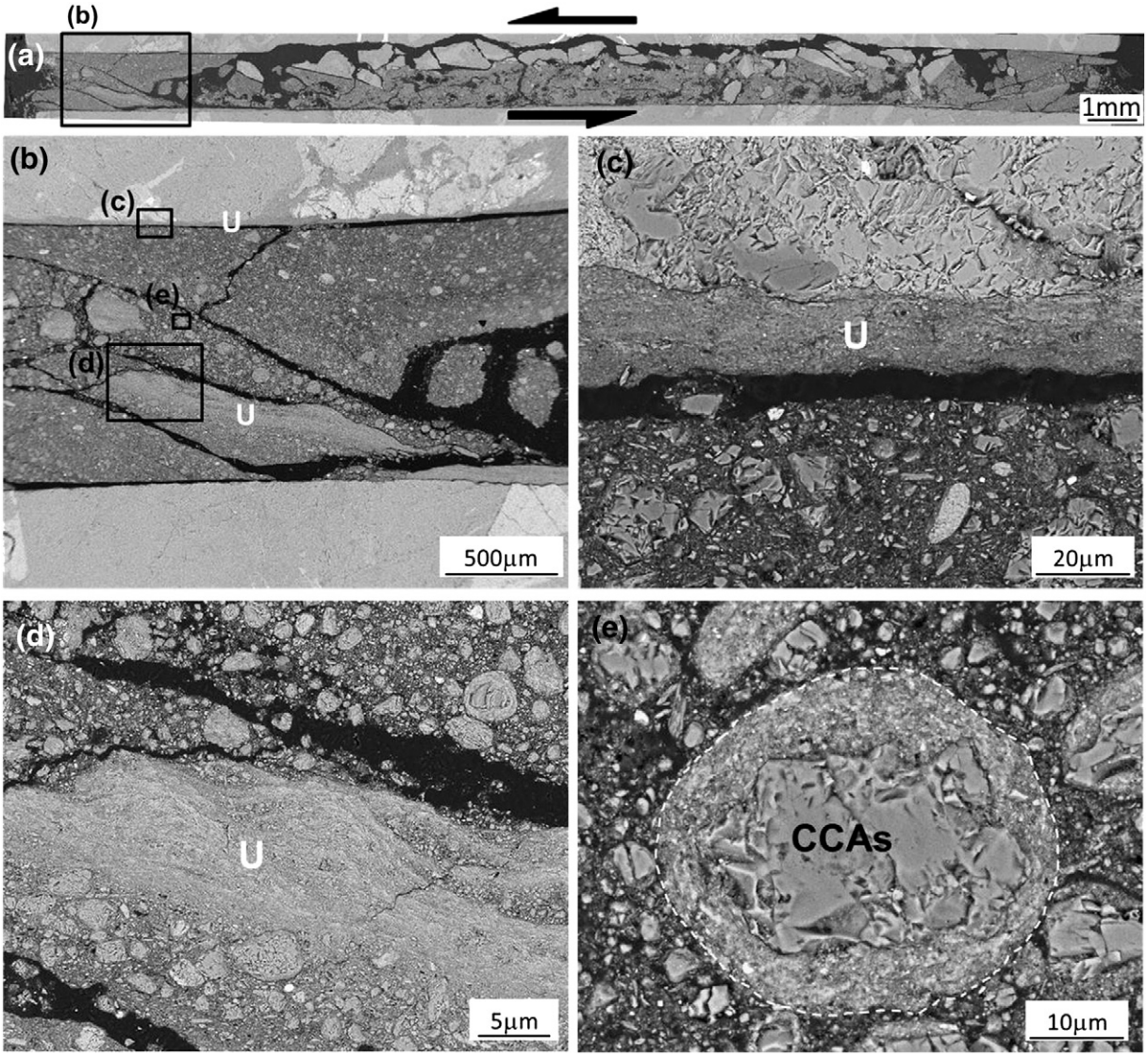


**Fig. 11.** Back-scattered electron images of fault gouge deformed at a normal stress of 3 MPa and a slip rate of 0.5 m/s (LHVR0129). (a) Photomicrograph showing the textures of the deformed fault gouge. (b) Detailed photomicrograph of the stratified fault gouge zone, including two U layers and spherical CCAs distributed throughout the fault gouge zone with the exception of the U layer. (c and d) The stratified fault gouge zone contains the upper and middle U layers and is mainly comprised of foliated minerals with few quartz grains. The middle U layer contacts the overlying CCA layer along a well-defined boundary, while the boundary between this fault gouge layer and the underlying CCA layer cannot be identified clearly. (e) Detailed photomicrograph of CCAs near the middle U layer.

weakening distance resulted from the decrease of the friction coefficient with increasing shear displacement. We speculate that the decrease in strength is due to the rapid generation of excess pore pressure. The tests of the semi-wet fault gouges (sheared after consolidation) yielded a larger $D_c$.

## 5. Initiation and kinematics of the Tsaoling landslide based on a rigid block model that incorporates a velocity–displacement dependent friction law

### 5.1. Newmark displacement method

This section reports our Newmark analysis of the Tsaoling landslide that incorporates the proposed velocity–displacement dependent friction law and the frictional properties summarized in the last two sections. We idealize the Tsaoling landslide as a rigid-block sliding on along a bedding plane dipping 14° in Stage I and along a slope dipping 20° in Stage II as summarized at the end of Section 2 (Figure 3b). Newmark (1965) proposed a procedure for evaluating the potential deformation of an earth dam due to earthquake shaking. The Newmark displacement analysis has been widely employed to investigate the initiation and kinematics of earthquake-induced landslides and to back-calculate strength parameters (Wilson and Keefer, 1983; Jibson and Keefer, 1993; Romeo, 2000; Huang et al., 2001; Lee, 2001; Sepúlveda et al., 2005; Wu and Tsai, 2011; Chen et al., 2014). Movement of a block (or landslide mass) is assumed to start when the ground acceleration exceeds a critical acceleration $A_c$. But here we use an acceleration of the sliding block $S$ derived by Huang et al. (2001):

$$S = (g\sin\theta - A_d) - \mu(g\cos\theta + A_n) \tag{6}$$

where $g$ is the acceleration of gravity, $\theta$ is the dip angle of the sliding surface, $\mu$ is the friction coefficient along the sliding surface, $A_d$ is the acceleration in the down-dip direction (positive downward), and $A_n$ is the acceleration normal to the sliding surface (positive upward). We neglected the cohesion term based on the results from friction experiments in the last two sections. The down dip velocity of the rigid block can be calculated easily by integrating the positive value of the

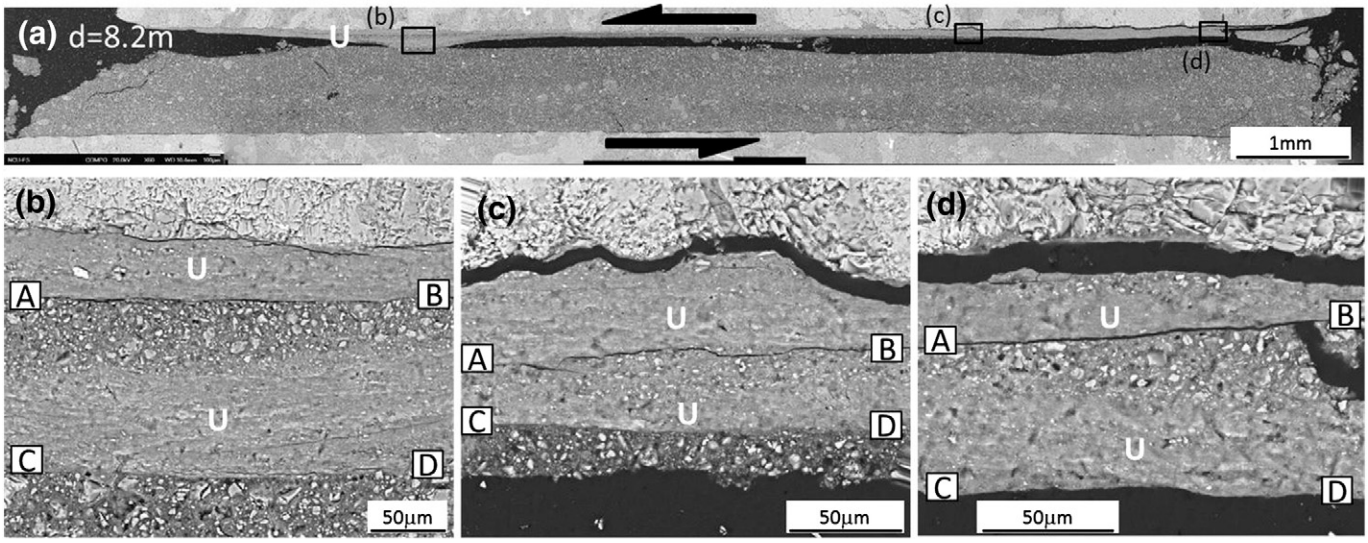


**Fig. 12.** Back-scattered electron images of fault gouge deformed at a normal stress of 3 MPa and a slip rate of 0.22 m/s (LHVR0259, transitional regime). (a) Photomicrograph showing the texture of the deformed fault gouge. (b to d) Two U layers above AB and CD observed at this scale. The U layer was separated by several groups of fine quartz particles across the entire section.

down-dip sliding acceleration $S$, and the permanent displacement of the sliding block can be obtained by integrating the velocity of the block.

Note that an upward movement of ground (or negative $A_d$) promotes landslide motion and increases $S$ (the first term in Eq. (6)). Moreover, an upward ground motion (or positive $A_n$) increases the normal stress on the sliding surface, thereby increasing the friction and decreasing $S$ (the second term). Traditionally, the critical acceleration $A_c$ is treated as a constant which can be expressed as the function of the friction angle (or friction coefficient) on the sliding surface ($A_c = [(\mu - \tan\theta)/(1 + \mu \tan\theta)]g$). Dong et al. (2009) utilized a velocity-dependent

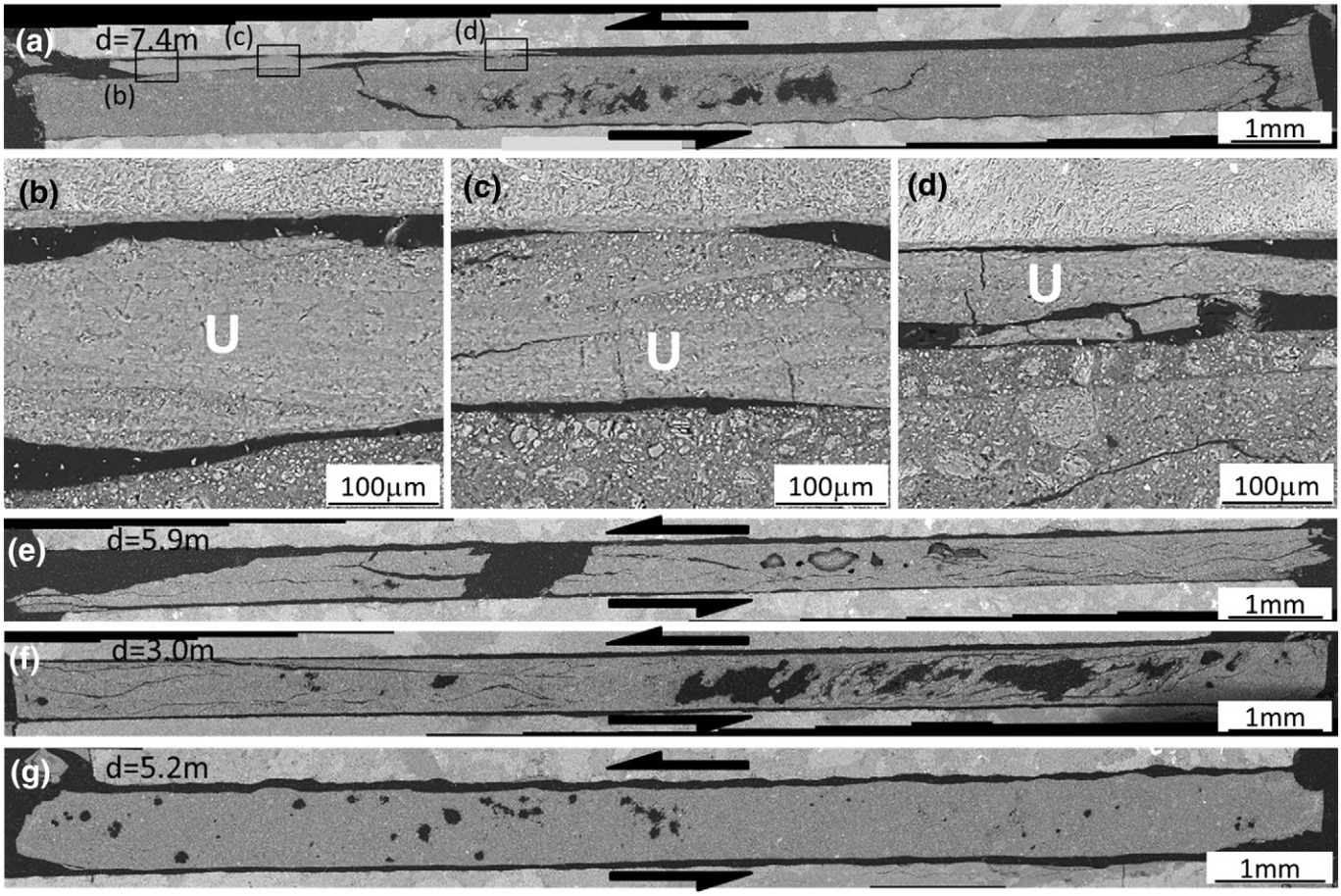


**Fig. 13.** Photomicrographs of samples from the slip-strengthening regime. The fault gouge was deformed at a normal stress of 3 MPa and a slip velocity of (a) 0.1 m/s (LHVR256). (b to d) These textures are similar to those in Fig. 12b to d but are less extensive (approximately 4 mm wide). The fault gouges were deformed at a normal stress of 3 MPa and slip velocities of (e) 0.0023 m/s (LHVR261), (f) 0.0124 m/s (LHVR262), and (g) 0.0436 m/s (LHVR254).

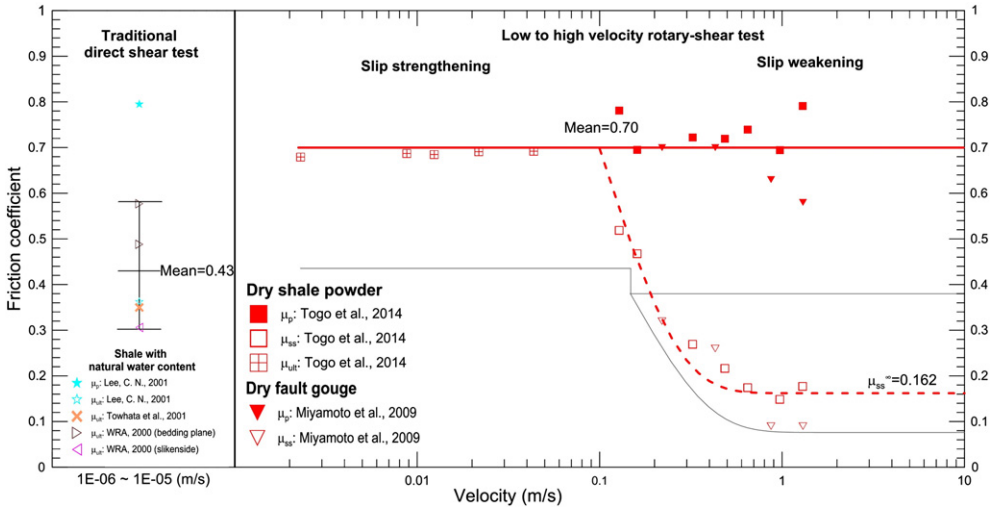


**Fig. 14.** Friction coefficients of dry samples collected from the Tsaoling landslide site reported by Miyamoto et al. (2009) and Togo et al. (2014). The squares and triangles represent the results from dry shale powders and dry fault gouges, respectively. The solid gray lines represent the curves fitted to the results of this study (Figure 8). The left part shows the friction coefficients of wet shales from traditional direct shear tests.

friction coefficient to calculate the temporal variation of the critical acceleration which is a function of the rigid block velocity. In this study, we use a displacement- and velocity-dependent friction law, Eqs. (2), (4), and (5), for $\mu$ in Eq. (6) with measured parameters summarized in the last two sections. The critical acceleration of the simulated rigid block is therefore velocity–displacement dependent. Marked slip- and velocity-weakening (reduction in $\mu$) increases $S$ causing high-speed catastrophic landslides.

Fig. 17a exhibits acceleration of the ground motion record during Chi-Chi earthquake recorded at station CHY080 (see Figure 1 for its location) that was used in our Newmark analysis of the Tsaoling landslide. The total duration of the earthquake signals recorded by CHY080 was 159 s, but the figures show only records of 25 s since the arrival of P waves, using the time since the generation of the Chi-Chi earthquake at its epicenter on the horizontal axis. The peak ground accelerations (PGA) were 715.9, 792.4, and 841.5 gal for the vertical, E–W, and N–S, components, respectively (Figure 17a; Lee et al., 2001). The P-wave and S-wave arrivals were 20.0 s and 25.2 s, respectively (Kuo et al., 2013). The site effects in the landslide source area may have also influence the analysis. However, the observation site is located at about the same elevation as the original landslide site on the same mountain, and we did not consider an amplification of the recorded ground accelerations in our calculations. Fig. 17b shows normal and down-dip accelerations $A_n$ and $A_d$ calculated from the acceleration records for the time periods of 30 to 45 s that are critical to the analysis of the Tsaoling landslide and are discussed in detail in the next subsection.

### 5.2. Rigid block modeling of the Tsaoling landslide using semi-wet fault gouge parameters

We now conduct a Newmark analysis of the Tsaoling landslide for Stages I and II, using the frictional parameters for the semi-wet fault gouge (Section 3). Parameters for the idealized velocity–displacement friction law are listed in Table 4 as Scenario 1, corresponding to our experimental data summarized in Fig. 8 (note that we used an average value of $D_c$ (4.9 m) in Table 1). Eqs. (2) and (4) with those parameters were incorporated into the friction coefficient term $\mu$ in Eq. (6) to calculate the time history of the down dip acceleration $S$ (gray curves), velocity $V$ (green curves), cumulative displacement $d$ (blue curves), and

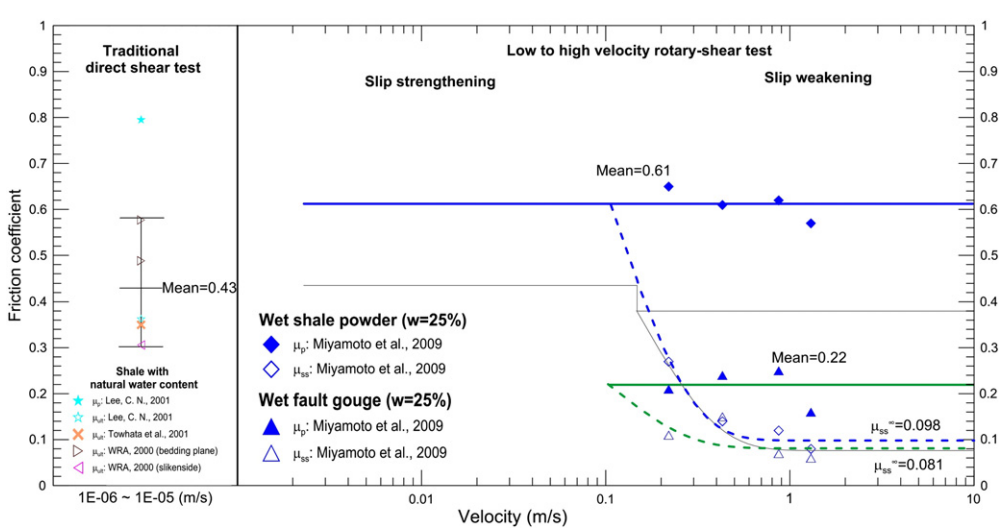


**Fig. 15.** Friction coefficients of wet samples collected from the Tsaoling landslide site reported by Miyamoto et al. (2009). The diamonds and triangles represent the results of wet shale powders and wet fault gouges, respectively. The solid gray lines represent the curves fitted to the results of this study (Figure 8). The left part shows the friction coefficients of the wet shales from traditional direct shear tests.

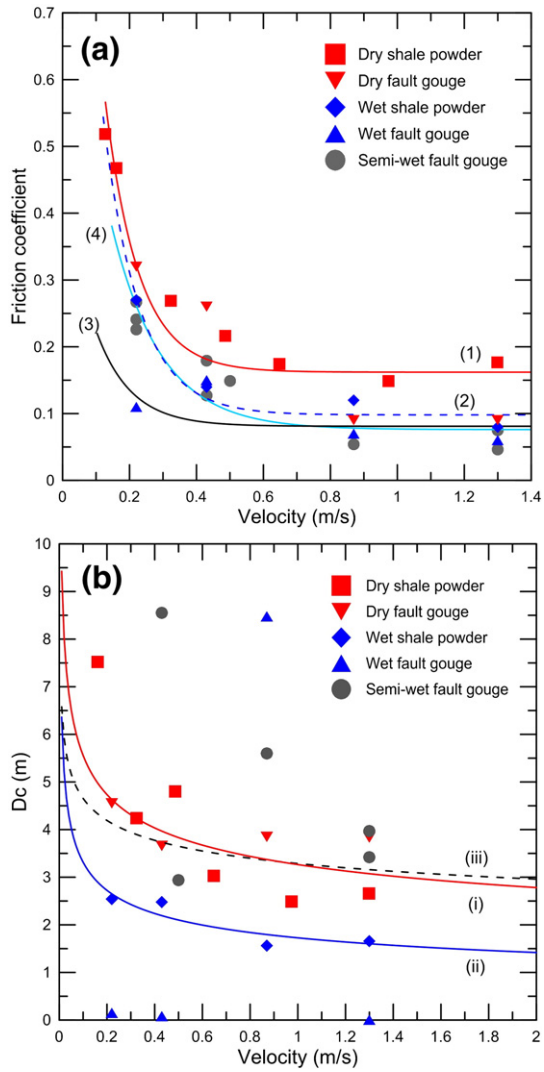


**Fig. 16.** (a) Steady-state friction coefficients ($\mu_{ss}$) of all of the datasets. The red line (1) represents the dry shale powder and fault gouge; the blue dashed line (2) represents the wet shale powder; the black line (3) represents the wet fault gouge; the blue solid line (4) represents the semi-wet fault gouge from this study. (b) Velocity dependency of slip-weakening distance. The red line (i) represents the dry samples; the blue line (ii) represents the wet shale powders; the black dashed line (iii) represents the fitted curve of all of the datasets (Togo et al., 2014: dry shale powder; Miyamoto et al., 2009: dry and wet fault gouge and wet shale powder; this study: semi-wet fault gouge).

friction coefficient $\mu(V)$ (red curves) in Fig. 18, using the time in seconds since the generation of the Chi-Chi earthquake on the horizontal axes. The result for the initiation portion of the landslide in Fig. 18a indicates that the landslide motion started at 31.6 s (a small pulse in the green curve on the lower-left side of the bottom diagram) where the down-dip acceleration $S$ became positive at this time to initiate the landslide motion (gray curve at 31.6 s in the figure). But the landslide motion stopped soon after the $S$ went back to negative again. There were five

**Table 2**
Parameters of the dry and wet samples in the velocity-dependent friction law.

| Materials | $\mu_{ult}$ | $\mu_p$ | $V_{Critical}$ [m/s] | $\mu_{ss}^{\infty}$ |
|---|---|---|---|---|
| (1) Dry shale powders and fault gouges (Togo et al., 2014) | 0.70 | 0.70 | 0.10 | 0.162 |
| (2) Wet shale powders (Miyamoto et al., 2009) | 0.61 | 0.61 | 0.11 | 0.098 |
| (3) Wet fault gouges (Miyamoto et al., 2009) | 0.22 | 0.22 | 0.10 | 0.081 |
| (4) Semi-wet fault gouges (this study) | 0.44 | 0.38 | 0.15 | 0.076 |

**Table 3**
Parameters of the dry and wet samples in the velocity dependent slip-weakening distance.

| Materials | $a$ [m] | $b$ |
|---|---|---|
| (i) Dry shale powders and fault gouges (Togo et al., 2014) | 3.27 | 0.23 |
| (ii) Wet shale powders (Miyamoto et al., 2009) | 1.73 | 0.28 |
| (iii) All datasets | 3.29 | 0.15 |

similar pulse-like movements before the onset of continuous sliding at 38.0 s, and they caused small step-like increase in the cumulative displacement $d$ (blue curve in Figure 18a). They correspond to positive peaks of $S$ above the dashed line for $S = 0$ in Fig. 18a. There are two small peaks between 32 s and 33 s, but the positive $S$ peaks are too small to cause corresponding velocity pulses visible in the figure. After 38 s the velocity $V$ increased and decreased twice, but $V$ did not go back to zero and the Tsaoling landslide was triggered. The accumulated displacement was 0.65 m. We thus take 38.0 s as the time for the onset of landslide since the generation of the Chi-Chi earthquake at its epicenter (denoted as $T_{Chi-Chi}$ in Table 4) and 0.65 m is the critical slip distance for the occurrence of an earthquake induced landslide. $T_{Chi-Chi} = 38.0$ s corresponds to 12.8 s after the $S$ wave arrival to the landslide site ($T_S$ in Table 4). Apparently, the landslide was triggered by a sharp spike in $S$ exceeding 1000 gal at 38.0 s that corresponds to the sharp negative peaks of $A_n$ and $A_d$ in Fig. 17 b, both promoting the landslide motion (note the effects of $A_n$ and $A_d$ on $S$ in Eq. (6)). Strong ground motion ended at around 41 s after which both normal and down-dip accelerations $A_n$ and $A_d$ decreased (Figure 17), but the down-dip acceleration $S$ of the landslide mass remained positive even after that. This was caused by the velocity- and slip-weakening of the sliding surface, i.e., the reduction in $\mu$ in Eq. (6) which allowed the continued high-speed landslide possible. Then the landslide mass went into Stage II at 69.3 s after the generation of the Chi-Chi earthquake with a velocity of 50.7 m/s and into Stage III at 82.2 s with 84.6 m/s (Figure 18b; Table 4, two columns on the right). A knee in the velocity curve at the boundary between Stages I and II is caused by the difference in the slope angles (14° and 20°, Figure 3b).

Friction coefficient $\mu$ along the sliding surface changes as the landslide velocity $V$ and the cumulative displacement $d$ changes as shown by red curves in Fig. 18. We assumed $\mu(V) = \mu_{ult}$ for sliding velocity $V$ less than a critical velocity $V_{Critical}$ (Figure 8), so that two small pulses of movements at 34 s and 36.5 s did not cause any changes in $\mu(V)$. The three larger pulses of movements at 34.6 s, 35.4 s, and 37.1 s caused reduction in $\mu(V)$ following the velocity- and displacement-dependent friction specified by Eqs. (2) and (4), but $\mu(V)$ went back to $\mu_{ult}$ as $V$ became zero (see the red curve corresponding to the pulses in Figure 18a). The landslide velocity $V$ increased to 2.3 m/s at 38.4 s and then decreased to 0.6 m/s at 38.9 s after the onset of landslide at 38 s, but this reduction in $V$ caused only a slight increase in $\mu(V)$ because $V$ was greater than $V_{Critical} = 0.15$ m/s (green and red curves in Figure 18a). The friction coefficient $\mu(V)$ quickly changes to $\mu_{ss}^{\infty}$ in a few seconds and $\sim \mu_{ss}^{\infty}$ after about 42 s (red curves in Figure 18a, b), and $\mu_{ss}^{\infty}$ essentially determines the landslide speed.

### 5.3. Rigid block modeling using existing friction data of shale powder and fault gouge

Based on the existing friction data summarized in Section 4 (Figures 14–16 and Tables 2–3), we set up Scenarios 2 to 6 with materials from the landslide site and their frictional parameters shown in Table 4. The critical velocity for the onset of marked slip-weakening $V_{critical}$ is fairly similar in all scenarios, but other frictional parameters vary considerably with different scenarios. Scenario 2 represents the case of a sliding surface that is composed of dry shale powders or dry fault gouges whose frictional properties (Miyamoto et al., 2009; Togo et al., 2014) are summarized in Figs. 14 and 16. The bedding-parallel fault gouges used in Miyamoto et al. (2009) were collected from the same fault zones as we collected our fault gouge samples. Shale is the

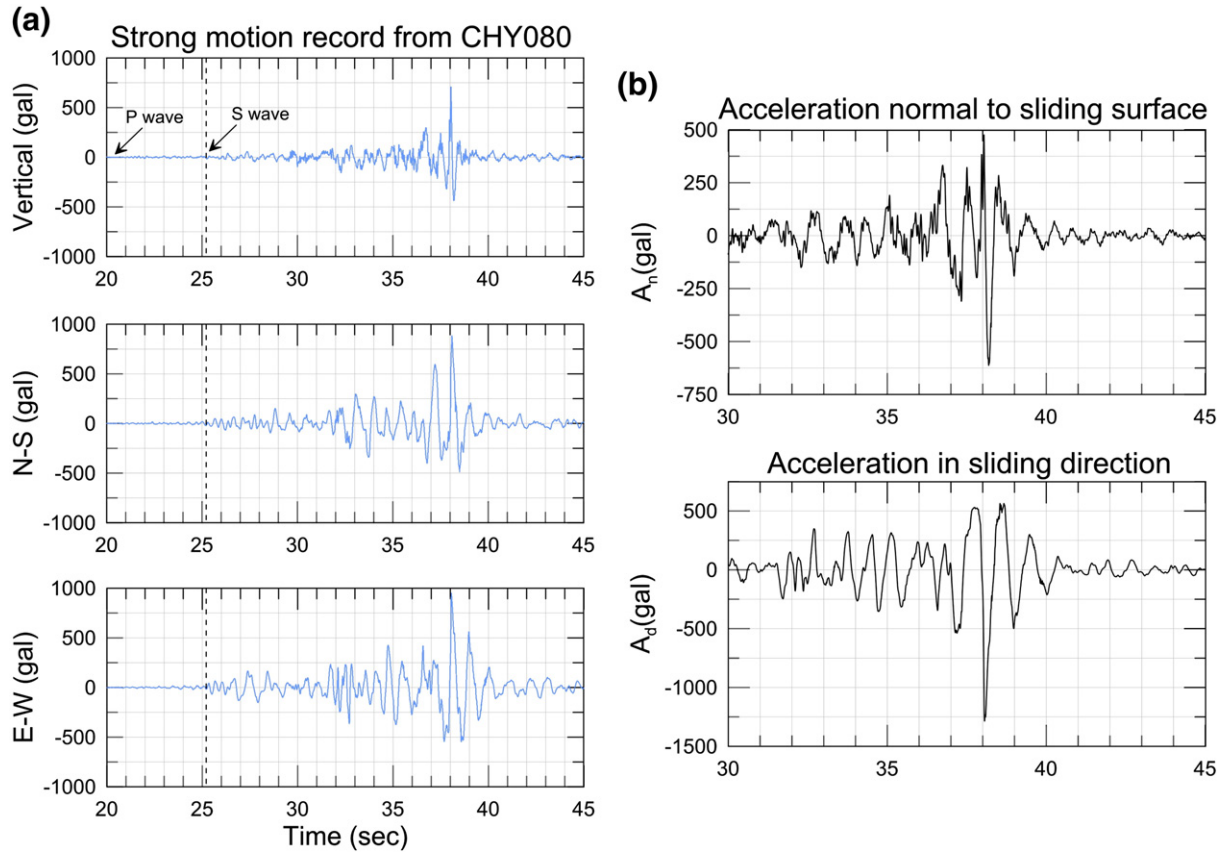


**Fig. 17.** (a) Ground acceleration in the vertical, N–S, and E–W directions during the 1999 Chi-Chi earthquake recorded with a sampling rate of 200 Hz at station CHY080, located about 700 m to the north from the original landslide site. (b) Calculated acceleration in the normal direction to the sliding surface ($A_n$, positive upward; top diagram) and acceleration in the sliding direction ($A_d$, positive downward; bottom diagram), using Eq. (3) in Huang et al. (2001). Figures show acceleration data only for the time periods that are important in landslide analyses.

weaker member of the alternated sandstone and shale, and is likely to determine the frictional strength of the bedding planes. Under dry conditions with room humidity, the shale powder and fault gouge exhibit similar frictional properties with the ultimate friction coefficient in the slip-strengthening regime $\mu_{ult} = 0.70$, peak friction coefficient $\mu_p = 0.70$, steady-state friction coefficient $\mu_{ss}{}^{\infty} = 0.162$, and slip-weakening distance $D_c = 3.27(V/V_0)^{-0.23}$ (Table 3, second row; Figure 16b). Values of $D_c$, $\mu_p$, and $\mu_{ss}{}^{\infty}$, are much larger than those in Scenario 1, and the Newmark analysis reveals three pulses of movements at 37.1 s, 38 s, and 38.9 s corresponding to three $S$ peaks above $S = 0$ line (Figure 19a), and the pulse-like motion caused a cumulative displacement $d$ of 0.66 m. The landslide motion stopped in Scenario 2 because the friction coefficient $\mu$ remained high and $S$ did not stay positive after the movements. This result is consistent with the result by Togo et al. (2014) using the frictional properties for the dry shale powder.

Scenario 3 is the wet shale powder whose frictional properties (Miyamoto et al., 2009) can be described by $\mu_{ult} = 0.61$, $\mu_p = 0.61$, $\mu_{ss}{}^{\infty} = 0.098$, and $D_c = 1.73(V/V_0)^{-0.28}$ (Table 4, third row; Figure 16b). Those friction coefficients are intermediate between those in Scenarios 1 and 2, but $D_c$ is smaller than those in the two scenarios (Figure 16b).

**Table 4**
A summary of frictional parameters for five scenarios and results of the Newark analysis of the Tsaoling landslide. $\mu_{ult}$: an ultimate friction coefficient in the slip-strengthening regime, $\mu_p$: peak friction coefficient, $\mu_{ss}{}^{\infty}$: steady-state friction coefficient at infinite velocity, $V_{critical}$: critical velocity for the onset of marked slip-weakening, $D_c$: slip-weakening distance, $a$ and $b$: parameters for the velocity dependence of $D_c$, $T_{Chi-Chi}$: time for the onset of Tsaoling landslide since the time of generation of the 1999 Chi-Chi earthquake at its epicenter, and $T_S$: time for the onset of the landslide since the S-wave arrival to the landslide area. The two numbers on the two columns on the right side give the arrival time since the generation of the Chi-Chi earthquake, and final velocity of the landslide mass at the ending points of Stages I and II.

| Scenario | Gouge types | $\mu_{ult}$ | $\mu_p$ | $\mu_{ss}{}^{\infty}$ | $V_{critical}$ [m/s] | $D_c$ [m] | | Landslide [s] $T_{Chi-Chi}/T_S$ | Accumulated displacement before initiation [m] | Arrival time [s]/ final velocity [m/s] | |
|---|---|---|---|---|---|---|---|---|---|---|---|
| | | | | | | $a$ [m] | $b$ | | | End of Stage I | End of Stage II |
| 1 | Semi-wet fault gouge(this study) | 0.44 | 0.38 | 0.076 | 0.15 | 4.9 | | 38.0/12.8 | 0.65 | 69.3/50.7 | 82.2/84.6 |
| 2 | Dry shale powders and dry fault gouges(Togo et al., 2014) | 0.70 | 0.70 | 0.162 | 0.10 | 3.27 | 0.23 | Landslide stopped. | | | |
| 3 | Wet shale powders(Miyamoto et al., 2009) | 0.61 | 0.61 | 0.098 | 0.11 | 1.73 | 0.28 | 38.9/13.7 | 1.09 | 72.8/47.5 | 86.8/80.5 |
| 4 | Semi-wet fault gouge(this study) | 0.44 | 0.38 | 0.076 | 0.15 | 8.55 | | 38.0/12.8 | 0.62 | 71.4/50.7 | 84.9/82.7 |
| 5 | Semi-wet fault gouge(this study) | 0.44 | 0.38 | 0.076 | 0.15 | 3.29 | 0.15 | 38.0/12.8 | 0.69 | 68.7/50.7 | 82.2/84.6 |
| 6 | Wet fault gouges(Miyamoto et al., 2009) | | 0.22 | 0.081 | 0.10 | <1 | | Slope is unstable. | | | |

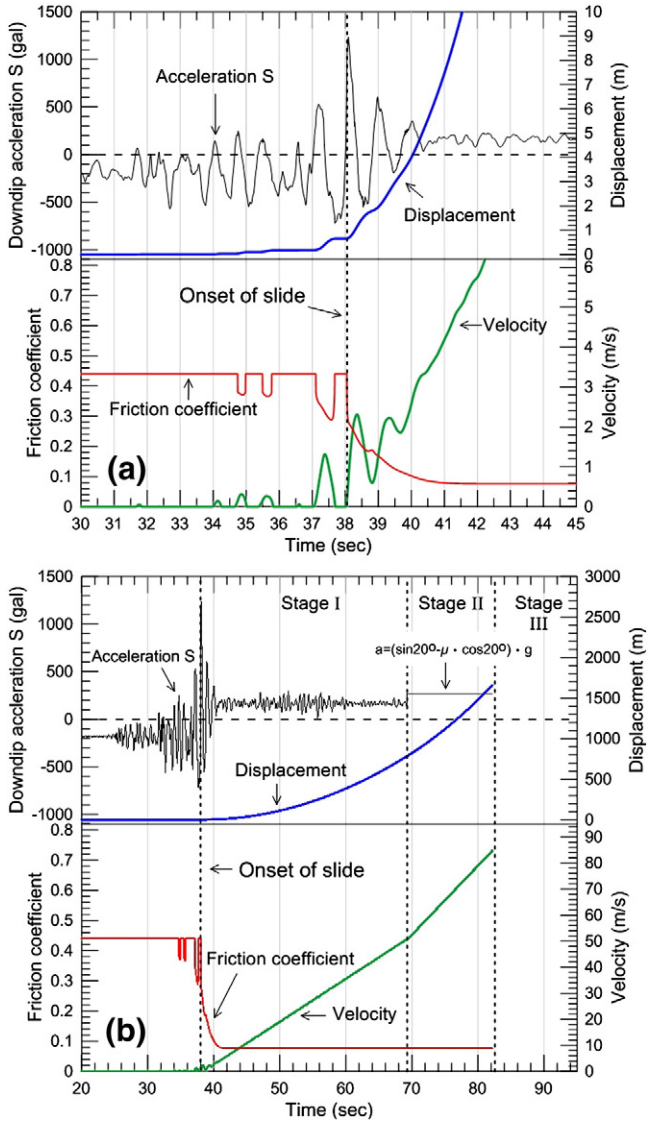


**Fig. 18.** Results of the Newmark analysis with the frictional parameters for the semi-wet fault gouge (a) for the initiation portion and (b) for Stages I and II of the Tsaoling landslide, showing time histories of the down-dip sliding acceleration $S$ (gray), velocity (green), and cumulative displacement (blue) of the moving block, and friction coefficient along the sliding surface (red). The horizontal axis gives time since the generation of the Chi-Chi earthquake at its epicenter. The horizontal dashed lines indicate $S = 0$ above which landslide motion takes place with an acceleration $S > 0$.

The result of the Newmark analysis in Figure 19b revealed that two pulse-like movements with accumulated displacement $d$ of 0.19 m and 1.09 m occurred at 37.1 s and 38.0 s corresponding to two positive $S$ peaks and that the landslide initiated at 38.9 s. That is, the critical slip distance of this scenario is 1.09 m. Several pulse-like movements as recognized in Scenario 1 did not occur because $\mu_{ult}$ was higher in Scenario 3 than in Scenario 1. This scenario appears to be very marginal in causing the Tsaoling landslide because the block of this case was not triggered by the sharp spike in $S$ exceeding 1000 gal at 38.0 s. The friction coefficient $\mu$ recovered back to the peak value of 0.61 after the largest spike of $S$ (red curve in Figure 19b). The block was triggered by the next spike follow the largest one and the $\mu(V)$ drops to $\mu_{ss}^{\infty}$ rapidly and a high-speed landslide occurs. The landslide motion after this is similar to that shown in Fig. 18a and we give only the time $t$ and velocity $V$ for the landslide mass to enter into Stage II ($t = 72.8$ s and $V = 47.5$ m/s) and into State III ($t = 86.8$ s and $V = 80.5$ m/s) in Table 4.

Scenarios 4 and 5 are for the semi-wet fault gouge as in Scenario 1, but we used a largest measured value to $D_c$ (8.55 m) in Scenario 4 and $D_c$ given by an equation that was fit to the whole data in Fig. 16b, $D_c = 3.29(V/V_0)^{-0.15}$, for Scenario 5 (fourth row in Table 3). The landslide motions in both scenarios are similar to that in Scenario 1 with several pulses of motion between 31.7 s and 37 s, ending up with the onset of landslide at 38.0 s with accumulated displacements of 0.62 m and 0.69 m (cf. Figure 19c, d, and Figure 18a). A large $D_c$ suppresses slip-weakening and the movement at 38 s stopped in Scenario 4, but it ran away at the next pulse of movement (Figure 19c). The landslide motions are quite similar between Scenarios 1 and 5 (cf. Figures 18a and 19d). Friction coefficient $\mu$ dropped to $\mu_{ss}^{\infty} = 0.076$ at about 44 s and 40 s in Scenarios 4 and 5, reflecting the difference in $D_c$ (cf. Figure 19c, d), but this much of difference does not change the high-speed landslide motion. The landslide mass went into Stage II at $t = 71.4$ s and $V = 50.7$ m/s and into Stage III at $t = 84.9$ s and $V = 82.7$ m/s in Scenario 4, whereas the times and speeds for Scenario 5 were $t = 68.7$ s and $V = 50.7$ m/s for State II and $t = 82.2$ s and $V = 84.6$ m/s for State III (Table 4, two columns on the right).

Scenario 6 is for the frictional properties of wet fault gouge (Miyamoto et al., 2009) with $\mu_p = 0.22$, $\mu_{ss}^{\infty} = 0.081$, and $D_c < 1$ m (Table 1, Figures 15, and 16). Although $\mu_{ult}$ is not reported in their paper, the friction angle for $\mu_p$ is 12.4° and is less than the slope angle of 14°. Thus the friction is not high enough to keep the Tsaoling landslide on the slope and the Newmark analysis cannot be done with this Scenario.

## 6. Discussion

### 6.1. Newmark analysis of the Tsaoling landslide

Previous studies on the Newmark analysis of landslides often assumed a critical slip distance of rock or soil slides (typically 50–100 mm), beyond which a slope instability might occur (Wieczorek et al., 1985; Keefer and Wilson, 1989; Jibson and Keefer, 1993). However, it has been unclear what determines the critical distance and how high-speed landslide initiates. Although the mechanisms that dominate the rapid and long run-outs of large landslides have not been conclusively determined (Hungr and Evans, 2004), Dong et al. (2013) attempted a Newmark analysis of the Tsaoling landslide using a block-sliding model with a velocity- and displacement-dependent friction law, describing marked slip-weakening behaviors of the landslide materials at high velocities. In this paper, we have expanded their analysis by presenting new experimental data on the fault gouge collected from bedding-parallel faults close to the sliding surface of the Tsaoling landslide (Section 3), by compiling existing friction data on the Tsaoling landslide materials (Section 4), and by modifying their velocity- and displacement-friction law (Eqs. (2), (4), and (5)). The Tsaoling landslide is an ideal case for such a study because the landslide occurred along a very flat bedding surface, particularly in Stage I (Figure 3b), and because the seismic records and a survivor's witness give constraints on the landslide motion. A high-frequency signal lasting for about 1 s was recorded at a nearby station CHY080 at 75.8 s after the generation of the Chi-Chi earthquake at its epicenter, and Kuo et al. (2009) proposed that these signals were caused by the impact of the Tsaoling landslide mass to the bank of the Chinshui River (point C in Figure 3b). Chen et al. (2014) recognized high-frequency signals at 32 to 40 s in the same seismic records and proposed that those are due to the initiation of the Tsaoling landslide.

In view of the geometry of the landslide surface along the sliding direction in Fig. 3b, we conducted the Newmark analysis for the rigid-block sliding during Stages I and II, before the landslide mass hit the river bank. One can argue that the sliding mass may not remain intact in Stage II because the two steps between B and C in Fig. 3b might have fragmented the landslide block. However, high-frequency signals were not recorded except for the two time periods quoted above, and

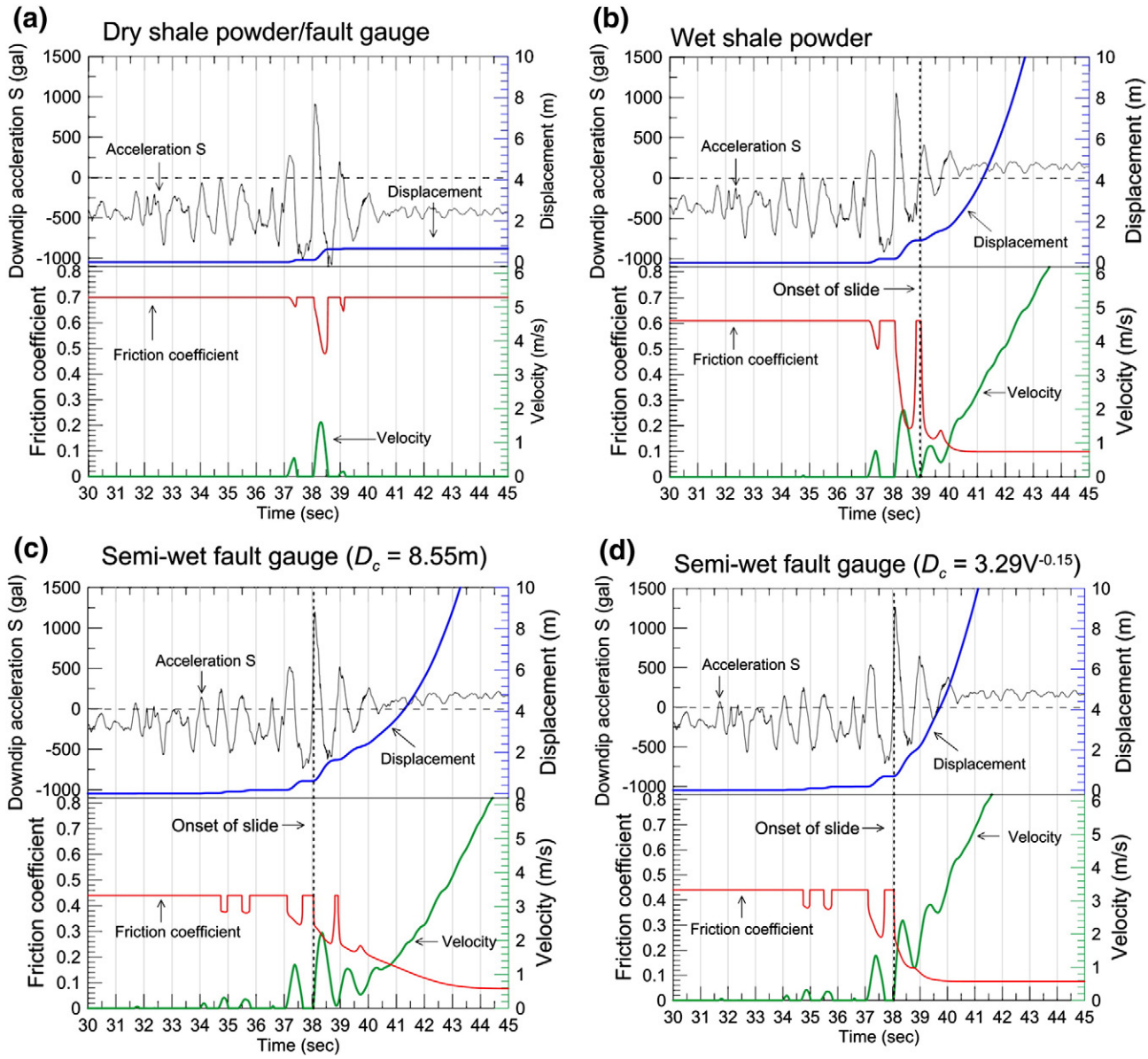


**Fig. 19.** Results of the Newmark analysis of the Tsaoling landslide (a) for Scenario 2 with the dry shale powder/fault gouge, (b) for Scenario 3 with the wet shale powder, (c) for Scenario 4 with the semi-wet fault gouge assuming $D_c = 8.55$ m, and (d) for Scenario 5 with semi-wet fault gouge assuming $D_c = 3.29(V/V_0)^{-0.15}$. Frictional parameters for the four scenarios are given in Table 4, and all figures are constructed similar to Fig. 18a. The horizontal dashed lines indicate $S = 0$ above which landslide motion occurs.

hence severe fragmentation of the landslide mass probably did not occur before it hit the river bank. Moreover, 39 people slid with the Tsaoling landslide mass over the Chinshui River and landed on top of the landslide deposits, and 7 people survived after sliding for a distance of 2250 m. Chen et al. (2014) reports an interview with a survivor who witnessed that "the sliding block remained more or less intact, especially in the rear part". Tang et al. (2009) also concluded that a chance for survival is low if the landslide mass disaggregated early in the sliding because of the extensive mixing of blocks, based on an analysis of the Tsaoling landslide using a discrete element method. Accordingly, the assumption of rigid body motion along the sliding plane in Stages I and II would be reasonable. However, the landslide mass must have broken into pieces after it hit the river bank to cover a wide area as shown in Fig. 3a. Alternative approaches such as an analysis using Voellmy rheology with a dynamic basal friction (Hungr and Evans, 1996, 2004; Pirulli and Mangeney, 2008; Sosio et al., 2008) may be applicable to the evaluation of the kinematics of disturbed landslide deposits, but the analysis of the stopping phase of the Tsaoling landslide is beyond the scope of this paper. However, we estimate later the loss of potential energy by the Tsaoling landslide and compare it with the frictional work during Stages I and II. This gives an estimate of the energy dissipated during the stopping phase of the landslide in Stage III.

We set up six scenarios using the frictional parameters determined for the experimental results on the shale powders and fault gouge under dry and wet conditions (Table 4). The landslide stopped after a few pulse-like movements in Scenario 2 for the dry shale powder and fault gouge because the ultimate friction coefficients in the slip-strengthening regime $\mu_{ult}$ and the peak friction coefficient $\mu_p$ were high (Figure 19a). The sliding surface was about 140 m below the surface at the time of Tsaoling landslide and probably was not under dry conditions because of frequent heavy rains in Taiwan. The other extreme case is Scenario 6 for wet fault gouge with $\mu_p = 0.22$ (or a friction angle of 12.4°), that is not high enough to keep the landslide mass on a slope dipping 14°. We will discuss a possible significance of this case in the next subsection in relation to rain-triggered landslides.

In all other scenarios, the landslide motion started either at 38.0 s or 38.9 s after the generation of the Chi-Chi earthquake at its epicenter, following a few to several pulse-like movements (Figures 18a, 19b–d; Table 4, column 9). The permanent displacements accumulated before the onset of the sliding were 0.62 ~ 1.09. P and S waves arrived in 20.0 s and 25.2 s, respectively, to the landslide site after the earthquake, so that the landslide occurred after 12.8 s or 13.7 s after the S-wave arrival in our Newmark analysis. A survivor witnessed to us that the Tsaoling landslide had started in about 10 s after he felt strong shaking. He did not measure this time interval with a watch or a clock, and his memory in such a chaotic situation may not be reliable. But nonetheless, our result for the landslide initiation is consistent with this witness if the seismic wave he felt was the S wave arrival (12.8–13.7 s versus 10 s). The timing of the landslide initiation in our analysis (pulse-like movements between 31.7 s and 38 s, and the onset of landslide at 38.0 or 38.9 s) agrees with the period of high-frequency signals at 32–40 s identified by the power-spectrum analysis by Chen et al. (2014). Finally, the landslide mass reached point C at 82.2–86.8 s after the generation of Chi-Chi earthquake (Table 4, column on the right side) and this timing is close to the timing of high-frequency signals at 75.8 s (Kuo et al., 2009). Friction coefficient $\mu$ drops to the steady-state friction coefficient at infinite velocity $\mu_{ss}^{\infty}$ in a few to several seconds after the onset of landslide (Figures 18 and 19b–d), so that $\mu_{ss}^{\infty}$ primarily determined the speed of a landslide. We assigned 0.076 or 0.098 for $\mu_{ss}^{\infty}$ based on the experimental results (Sections 3 and 4). However, it should be kept in mind that the high-velocity friction experiments have been conducted at velocities up to 1.3 m/s, more than one order of magnitude smaller than the speed of landslide. The values of $\mu_{ss}^{\infty}$ are extrapolated values to higher velocities. Moreover, an accurate measurement of $\mu$ below 0.1 is not easy because a precise correction of the measured shear stress for the friction between the Teflon sleeve and rotary specimen is required (see Sawai et al., 2012, Appendix). Despite those uncertainties, we consider that our Newmark analysis using experimentally-determined friction parameters successfully captured the initiation and movement processes of the Tsaoling landslide.

### 6.2. Friction constitutive law and importance of water

We now compare different friction models by previous workers and our friction law with different scenarios in this paper (Figure 20). The friction coefficients determined in the back calculations by Tang et al. (2009) with a discrete element method and by Kuo et al. (2009) using a continuum model of hydraulic flow are shown by orange and brown dashed lines, respectively, in Fig. 20a. Those methods are flexible in handling disaggregated particles such as debris flow and are powerful tools in solving the overall dynamic motion of high-speed landslides. However, the Tsaoling landslide mass cannot stay at a slope dipping 14° with the friction coefficients of 0.15 and 0.09 obtained in those studies, and hence the initiation processes of landslides cannot be solved by the methods. But the steady-state friction coefficients at infinite velocity $\mu_{ss}^{\infty}$ from this study (0.076 and 0.098) are comparable to the back-calculated basal friction values of 0.15 and 0.09.

All other methods summarized in Fig. 20 are the Newmark analysis with a few different friction laws. Chen et al. (2014) recently attempted to combine results from traditional direct shear tests and from high-velocity friction experiments by Miyamoto et al. (2009), and set up three levels of friction coefficient as shown by the green curve in Fig. 20a. They assumed that the peak friction coefficient (0.37) with cohesion of 152 kPa instantly dropped to the residual friction coefficient (0.24) as soon as sliding began and that the residual friction coefficient dropped instantly to the mobilized friction coefficient (0.05) after a displacement of 0.5 m (they studied the cases for $\mu_p$ of 0.58, 0.47, and 0.27 too). The mobilized friction coefficient corresponds to our steady-state friction coefficient $\mu_{ss}$ and was taken from Miyamoto et al. (2009). Although the Newmark analysis yielded similar results to ours in this study, such two abrupt changes in friction were not observed in any previous experiments. We do not consider that idealized behavior by Chen et al. (2014) is realistic.

Differences among other cases reflect either (1) difference in the friction law or (2) differences in the landslide materials and/or conditions. As for the friction law, Dong et al. (2013) used an exponential slip-weakening law, Eq. (2), with slip-weakening parameters given by Eqs. (3) and (5), for the experimental data by Miyamoto et al. (2009). The only difference between Dong et al. (2013) and the present study is that Dong et al. (2013) used Eq. (3) for the steady-state friction coefficient $\mu_{ss}$, whereas we used Eq. (4) with an additional parameter $\mu_{ult}$ (an ultimate friction coefficient in the slip-strengthening regime) in addition to the peak friction coefficient $\mu_p$ (Figures 8, 14, and 15). Thus this paper attempted to include the changes in friction with increasing slip rate (Figure 8), but the velocity dependency of friction is variable (e.g., Di Toro et al., 2011) and Eq. (4) is not general. A common feature of Eqs. (3) and (4) is that the steady-state friction coefficient $\mu_{ss}$ is forced

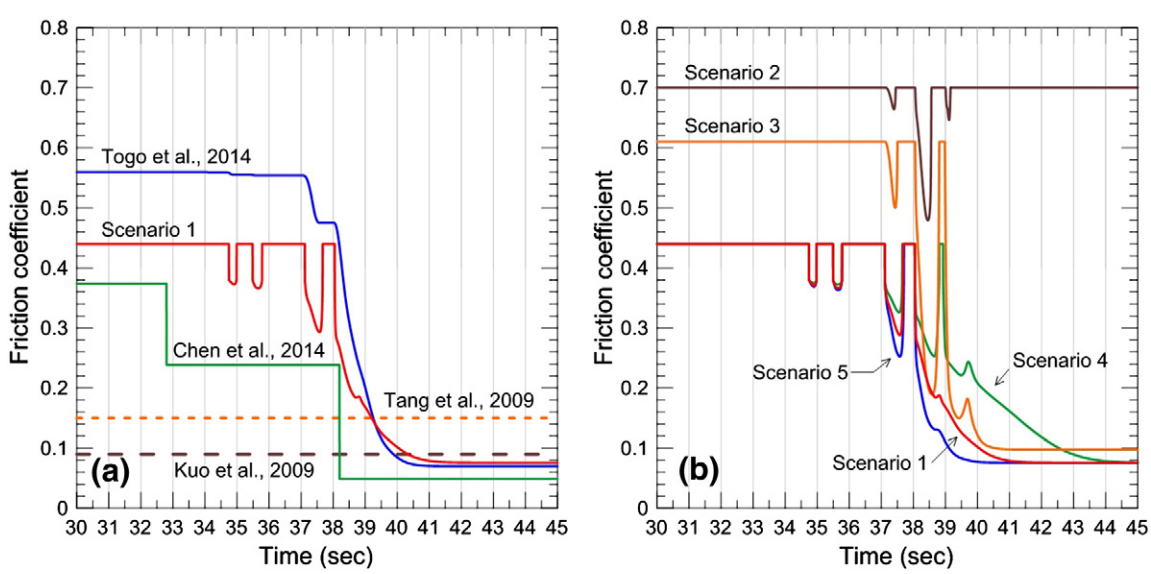


**Fig. 20.** (a) Temporal variation of the friction coefficient proposed by different researchers as shown on each curve, and (b) a comparison of temporal evolution of the friction coefficient for the five scenarios solved in this paper. Time on the horizontal axes gives the time after the generation of the 1999 Chi-Chi earthquake at its epicenter.

back to $\mu_p$ in Dong et al. (2013) and to $\mu_{ult}$ in our friction law as soon as the landslide velocity $V$ drops to zero. Because of this, the friction coefficient $\mu$ went back to the high initial values as $V$ decreased during the initial pulse-like movements (see results for Scenarios 1 and 3–5 in Figure 20b). Results by Dong et al. (2013) exhibit similar trends although we do not show their results in the figure.

On the other hand, Togo et al. (2014) idealized the early motion of earthquake-induced landslide as linear accelerating/decelerating slip and conducted friction experiments on dry shale powder from the Tsaoling landslide site with frequencies of 0.3 to 1.2 Hz. This slip history is very similar to the pulse-like early movements in the results from Newmark analysis in Figs. 18 and 19, except that there are temporary periods of stops between the accelerating/decelerating slip in the landslide motion (e.g., see five pulses of movements between 34 s and 38 s, separated by stops lasting 0.4–0.8 s in Figure 18a). Experimental results by Togo et al. (2014) revealed that the accelerating and decelerating motion caused weakening and strengthening, while undergoing overall slip-weakening. They approximated the overall behavior by an exponential weakening law, Eq. (2), and conducted the Newmark analysis of the Tsaoling landslide with results similar to those of our Scenarios 2 and 3 (Figure 19a, b). The change in $\mu$ in Togo et al. (2014) for wet shale powder is shown as blue line in Fig. 20a. This result without strength recovery is more realistic than those with our friction law in view of the results from the oscillatory accelerating/decelerating experiments, and the simple weakening law in Togo et al. (2014) would be better for analyzing the initiation of landslide. However, Togo et al. (2014) did not include changes in slip-weakening parameters with increasing velocities which reduces $\mu_{ss}^{\infty}$ and $D_c$. Thus, friction laws in this study and in Dong et al. (2013) are more involved in analyzing the high-speed landslide motion which is dictated by $\mu_{ss}^{\infty}$. Empirical approaches are inevitable at this stage until a constitutive law that can describe changes in friction for arbitrary slip histories at high velocities is proposed in the future.

Our results for six scenarios in Table 4 highlight the effects of frictional parameters and landslide materials. Dry shale powder and fault gouge has high $\mu_{ult}$ and $\mu_p$ (Scenario 2 in Table 4) and the landslide motion stopped after a few pulse-like movements (Figure 19a). But wet shale powder has lower values of $\mu_{ult}$, $\mu_p$, and $D_c$ (Scenario 3), making it possible to induce a landslide (Figure 19b). Semi-wet fault gouge has even smaller values of $\mu_{ult}$, and $\mu_p$ than those for the above cases and landslides occurred in Scenarios 1, 4, and 5 with different $D_c$ (Table 4, Figures 18, and 19c, d). Because of low $\mu_{ult}$ and $\mu_p$, the landslide mass is easy to move and the pulse-like motion started earlier than for wet shale powder cf. Figure 19b, c, and d). A large $D_c$ in Scenario 4 slowed down the reduction in $\mu$ with time (cf. green curve with the three curves for Scenarios 1, 3, and 5 in Figure 20b). Our analysis thus demonstrated that the landslide mass began to move at 31.7 s for semi-wet fault gouge and at 34.7 s for wet shale power after the generation of the Chi-Chi earthquake at its epicenter, and that the high-speed landslide started at 38.0 s for semi-wet fault gouge and at 38.9 s for wet shale powder. The calculated early movements are consistent with the high-frequency signals at 32 to 40 s analyzed recently by Chen et al. (2014). The landslide mass is likely to have hit the river bank at 75.8 s as suggested by the seismic record (Kuo et al., 2009). If the leading edge of the landslide mass in Fig. 3b caused the seismic signals, the sliding distance becomes about 1340 m and the average speed of landslide mass becomes about 36 m/s. Whereas if the high-frequency seismic record corresponds to the collision of the centroid of the mass, the sliding distance and the average speed become 1655 m and 44 m/s, respectively. It is hard to imagine that the collision of the frontal part of the landslide mass did not cause any signals, and we consider 35–40 m/s as a proper range of the average speed of the Tsaoling landslide mass during Stages I and II.

It is notable from Figs. 18–20 that the landslide can be triggered for fairly wide ranges of peak or ultimate frictional strength, $\mu_p$ or $\mu_{ult}$, and this was possible because of high accelerations to make the acceleration of the landslide mass $S$, given by Eq. (6), positive. However, another important factor is the amount of slip displacement of the landslide mass to reduce the friction angle below the slope angle to trigger the landslide. Fig. 21a–c exhibits seismic records for the critical time period, 35–40 s, in triggering the Tsaoling landslide, and Fig. 21d and e shows calculated accelerations, $A_n$ and $A_d$, in the normal direction to the sliding surface and in the down-dip direction, respectively. The strike and dip of the sliding surface of the Tsaoling landslide is 136° from N (clockwise) and 14° to SW, respectively, and Eq. (3) in Huang et al. (2001) gives:

$$A_d = -0.70 \cdot a_E - 0.67 \cdot a_N - 0.24 \cdot a_V, \quad (7)$$
$$A_n = -0.17 \cdot (a_E + a_N) + 0.97 \cdot a_V$$

where $a_E$, $a_N$, and $a_V$ are accelerations in the E–W, N–S, and vertical directions, respectively (eastward, northward, and upward positive). Eq. (6) for $S$ indicates that negative $A_n$ and $A_d$ increase $S$ and promote landslide motion. There are three positive $a_N$ peaks at 37.2 s, 38.1 s, and 39.0 s (Figure 21b), and $a_E$ has a broad positive peak at around 37 s and two positive peaks at 38.05 s and 39.0 s (Figure 21c). Those three positive peaks of $a_N$ and $a_E$ caused three negative $A_d$ peaks and three notable positive peaks of $S$, at around 37.2 s, 38.1 s, and 39 s (Figure 21f). Negative values of $A_n$ at 36.9–37.4 s, 38.1–38.4 s, and 38.9–39.2 s also contributed to the three positive $S$ peaks. Large down-dip acceleration $S$ allowed large enough displacement to reduce friction angle below the slope angle, over a slip-weakening distance $D_c$. Thus, the three $S$ spikes were large enough to trigger the Tsaoling landslide for a fairly wide range of $D_c$ values (up to 8.55 m, Table 4). Apparently, the Tsaoling landslide was triggered by the three strong acceleration pulses in the NE direction at 37–39 s, and unfortunately this was the most favorable orientation to induce the Tsaoling landslide. Forecasting such dangerous seismic ground motion from existing active faults would be the most important task in forecasting earthquake-induced landslides in the future.

Finally, it should be kept in mind that the cohesion term is not included in Eq. (6). How intact bedding planes develop into sliding surface with a small or negligible cohesion is an important problem to be studied experimentally. Repeated earthquakes such as the Chi-Chi earthquake might have caused small pulse-like movement to condition the bedding planes to change into easy sliding surfaces during geological time. Moreover, wet fault gouge has a friction angle smaller than the slope angle and cannot support the landslide. We added 25% of water to fault gouge and compacted the gouge under the same axial stress until the axial shortening stopped. Thus, part of water was squeezed out because the specimens were not sealed and this is the reason why we called our fault gouge as "semi-wet" gouge. On the other hand, Miyamoto et al. (2009) conducted friction experiments immediately after setting up the gouge with water, and this is probably the main reason for having higher values of $\mu_p$ and $\mu_{ult}$ in our experiments than in their results. We consider that our case is closer to the formations at the Tsaoling landslide site because there is enough time for excess water to escape from the sliding surface in nature. However, landslides were triggered at the Tsaoling landslide site by heavy rains in 1942 and 1979 (Hung et al., 2002). Heavy rain might have provided excess water into the sliding surface to reduce its friction. Effect of water on friction is very subtle and better controlled experiments on the effects of water are needed in the future. The effect of water is discussed further in the next subsection.

### 6.3. Microstructures of deformed gouge

The friction behaviors of samples with different water contents are quite different. Based on the microstructural observations in this study (Section 3.4), the semi-wet fault gouges sheared at high to low velocities contain a large variety of microstructural features from stratified to uniform (Figures 9 to 13). In contrast, the microstructures of the slip zone in wet samples do not change significantly by shearing at

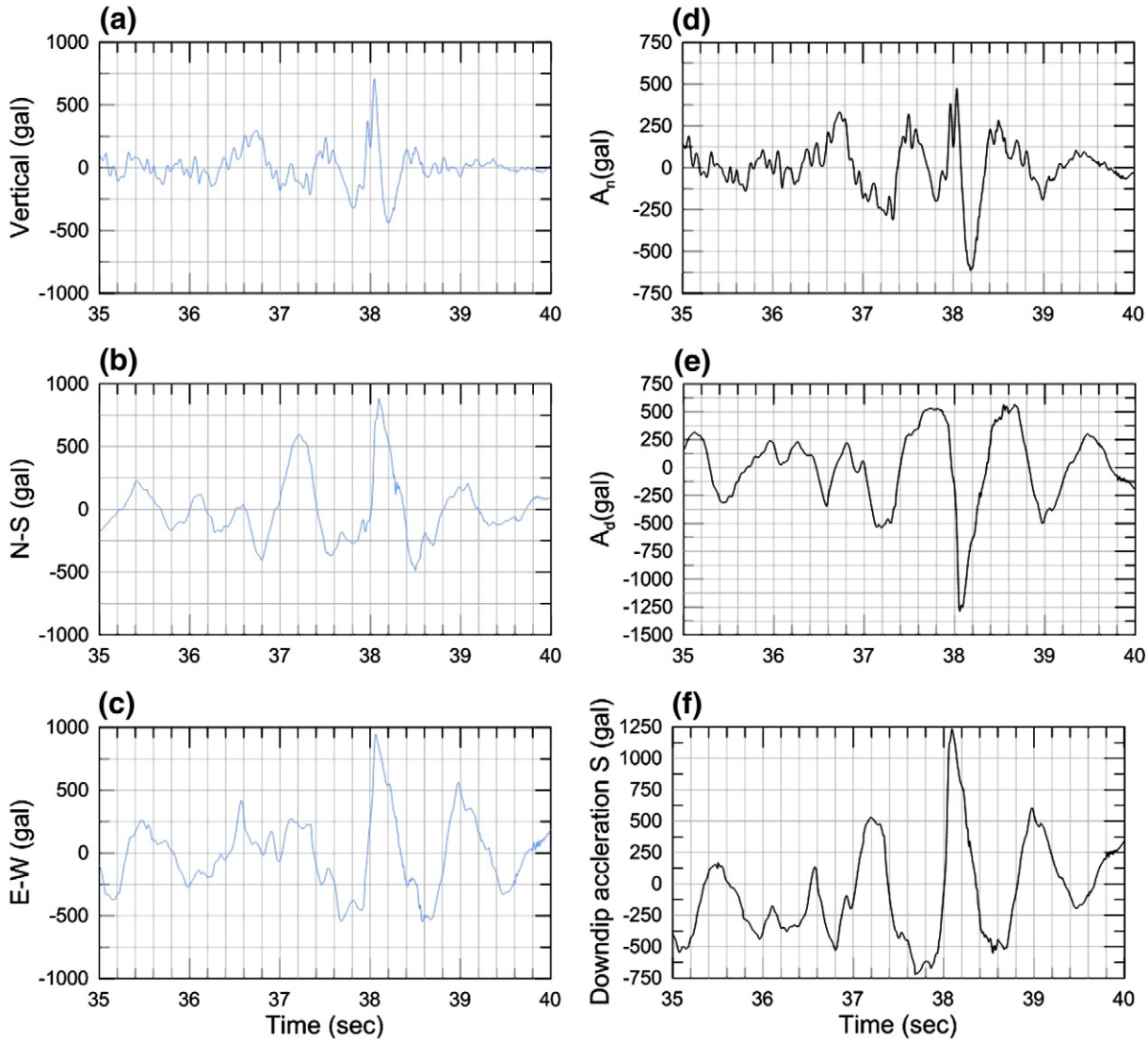


**Fig. 21.** Seismic ground motion during the critical time period of 35 to 40 s since the generation of the Chi-Chi earthquake, in triggering the Tsaoling landslide. Accelerations (a) for the vertical, (b) for the N–S, and (c) for the E–W directions, respectively, recorded at seismic station CHY080. (d) and (e) show calculated accelerations from (a) to (c) in the normal direction to the sliding surface and in the sliding direction, respectively. (f) Calculated acceleration of the landslide mass using the frictional parameters for Scenario 1 (see Table 4).

different velocities (Ferri et al., 2011). The microstructures of the wet samples were identified as insignificant shape-preferred clast orientations within a strongly foliated matrix. The foliation was locally deflected around the clasts, inclined towards the shear direction, and converged towards the shear localization zone that developed along the fault gouge-rock boundary. CCAs were not present in the sheared wet fault gouge samples at short shear displacements (<3 m) but appeared at large shear displacements, even in wet samples (Han and Hirose, 2012).

The wet clay-rich fault gouge ($w = 40\%$) was compacted, and water was progressively expelled along a continuous water film that formed at the clay-gouge/wall rock boundary (Ferri et al., 2011). Consequently, the peak friction coefficients of the wet samples are lower than those of the dry samples due to the lubrication of the water film. Another explanation is related to the excess pore pressure that is generated during loading. The degree of saturation dominates the generation of the excess pore pressure when a normal stress is applied. Higher initial water contents could give rise to higher excess pore pressures in the fault gouges, and the shear resistance will decrease accordingly. The peak friction coefficient will decrease with increasing water content of the tested sample. Because the effective stress does not change if the test occurs under saturated undrained shear conditions, similar microstructures are reasonable.

Based on rotary shear tests of dry fault gouge samples, Yao et al. (2013a) reported that a fine-grained deformation zone forms in the upper part of the fault gouge layer near the rotational side of the host rock with a slip displacement of 0.13 m at a normal stress of 2.5 MPa and a slip rate of 0.0014 m/s. Single or overlapping stratified structures of the U layer, CCA-bearing layers, and CCA-free layers were observed in air-dried samples and wet samples after large shear displacements (Boutareaud et al., 2010; Ferri et al., 2011; Han and Hirose, 2012; Sawai et al., 2012; Yao et al., 2013a, 2013b). In conclusion, the microstructures of our sheared semi-wet fault gouges are similar to those of the dry samples. This accounts for the similar steady-state friction coefficients of the samples with different water contents (Figures 14 and 15). We infer that the water contents of the tested samples decreased to low values similar to those of dry samples after large shear displacements.

An interesting result is that the slip-weakening is closely related to the appearance of the CCAs. Natural CCAs have frequently been observed in BSIs in association with carbonate-rich or smectite-rich fault rocks (Warr and Cox, 2001; Beutner and Gerbi, 2005; Boullier et al., 2009). Artificial CCAs have been produced from high-velocity rotary shear tests during investigations of fault dynamics (Boutareaud et al., 2010; Ujiie and Tsutsumi, 2010; Han and Hirose, 2012; Sawai et al.,

2012) and studies of catastrophic landslides (Ferri et al., 2011). The presence of CCAs indicates a liquid-vapor phase transition of pore-water and the interplay of complex physical and chemical processes (Boutareaud et al., 2010). CCAs tend to form in long run-out, large landslides where the shear displacement is large enough to raise the temperature to water vaporization or mineral decomposition conditions. Notably, the appearance of CCAs does not guarantee the onset of thermal pressurization (Ferri et al., 2011). Hungr and Evans (2004) summarized several possible mechanisms that may account for the weakening strength of large landslides. Davies and McSaveney (2009) suggested that the apparently instantaneous pressures resulting from grain fragmentation greatly reduces the effective stress, and the strength subsequently decreases. The mechanisms involved in the strength variations during large landslides can be complex (Legros, 2002), and further studies are required.

### 6.4. Energy budget of the Tsaoling landslide

Results from our study provide the interesting information on the energy budget of the Tsaoling landslide. The DTMs before and after the 1999 Chi-Chi earthquake revealed the horizontal travel distance $L$ of 2524 m and the elevation difference $H$ of 524 m during the Tsaoling landslide (Figure 3b), which gives an apparent friction coefficient of 0.21. The potential energy $E_p$ released during the Tsaoling landslide is given by:

$$E_p = m \cdot g \cdot H \tag{7}$$

where $m$ is the landslide mass, $g$ is the acceleration of gravity (9.807 m/s$^2$). The volume of the Tsaoling landslide is estimated at $1.25 \times 10^8$ m$^3$ (Tang et al., 2009) and Hung (1982) reports 2430 kg/m$^3$ for the density of rocks in Cholan formation. Those values give $E_p = 1.56 \times 10^{15}$ J.

On the other hand, we analyzed the Tsaoling landslide as a rigid block sliding in Stages I and II in Fig. 3b. After the onset of landslide, the friction coefficient $\mu(V)$ drops to the steady-state friction coefficient at infinite velocity $\mu_{ss}{}^{\infty}$ after sliding of a few to several seconds (red curves in Figures 18 and 19). Then the frictional work $E_f$ during the sliding is given approximately by:

$$E_f \approx mg\mu_{ss}{}^{\infty}(L_1 \cos\theta_1 + L_2 \cos\theta_2) \tag{8}$$

where $L_1$ and $L_2$ are sliding distances along the sliding surface (784 m and 871 m), and $\theta_1$ and $\theta_2$ are dip angles of the slopes (14° and 20°) for Stages I and II, respectively (Figure 3b). Those values and $\mu_{ss}{}^{\infty} = 0.076$ gives $3.58 \times 10^{14}$ J. Thus the frictional work $E_f$ is only 23% of the released potential energy $E_p$ of the Tsaoling landslide, and most of $E_p$ must have been consumed in Stage III such as crushing of the landslide mass and heat dissipation. Analysis of particle size distribution of the Tsaoling landslide deposits is interesting in estimating the energy used for the fragmentation of the landslide mass, but studying the complex landslide processes in Stage III is beyond the scope of this paper.

## 7. Conclusions

We conducted rotary-shear high-velocity friction experiments on fault gouge from bedding-parallel faults immediately below the sliding surface of the Tsaoling landslide induced by the 1999 Chi-Chi earthquake, compiled existing friction data on the Tsaoling landslide materials, proposed a revised friction law that can describe the velocity–displacement dependent frictional behaviors, and performed Newmark analysis of the triggering and high-speed sliding of the Tsaoling landslide using the experimentally-determined frictional properties. The main outcomes from this study are summarized below.

(1) Frictional behavior of the semi-wet fault gouge in our rotary-shear experiments can be described by a few empirical equations using the ultimate friction coefficient in the slip-strengthening regime $\mu_{ult}$ (0.44), peak friction coefficient $\mu_p$ (0.38), steady-state friction coefficient at infinite velocity $\mu_{ss}{}^{\infty}$ (0.076), critical velocity for the onset of dramatic slip-weakening $V_{Critical}$ (0.15 m/s), and by the slip-weakening distance $D_c$ (4.9 m on the average). The same parameters were compiled for reported frictional properties of shale powder and fault gouge from the Tsaoling landslide site under dry and wet conditions, to determine variations of frictional properties. Deformation textures of the semi-wet gouge are similar to those reported for dry fault gouges, but their frictional strength is smaller than that of dry gouges.

(2) We classified the Tsaoling landslide motion into three stages; i.e., Stage I — rigid-block sliding on a flat bedding place dipping 14°, Stage II — nearly rigid-block sliding on a steeper surface dipping 20°, and Stage III — stopping phase after the hitting of the landslide mass against the bank of the Chinshui River. We performed Newmark analysis of landslide motion in Stages I and II, assuming rigid-block sliding and using measured frictional properties with five scenarios set up for shale powder and fault gouge under dry, semi-wet and wet conditions.

(3) Our Newmark analysis showed that the landslide stopped after a few pulse-like motions with frictional properties for dry shale powder and fault gouge. But analysis for the other four scenarios for wet shale powder and fault gouge revealed that the landslide motion started at 38.0 or 38.9 s after the generation of the earthquake at its epicenter, following a few to several pulse-like motions. This is consistent with high-frequency signals at 32–40 s reported by Chen et al. (2014) who suggested that the signals are associated with the initiation of the landslide. The onset of landslide was at 12.8 s or 13.7 s after the S wave arrival to the landslide site, and our results agree with a survivor's witness that the landslide started in about 10 s after he felt a strong earthquake, possibly due to S wave. Our analysis showed that the landslide mass reached the river bank at 82.2–86.8 s after the generation of Chi-Chi earthquake and this is very close to the high-frequency signals at 75.8 s reported by Kuo et al. (2009) who proposed that the signals are due to hitting of the landslide mass against the river bank. Thus, our analysis reproduced the overall features of the Tsaoling landslide remarkably well with measured frictional properties. A typical average speed of the Tsaoling landslide during Stages I and II is 35–40 m/s. It is interesting to note that the evaluated critical slip distance were from 0.62 m to 1.09 m, which is considerably larger than the documented one for shallow slides.

(4) The sliding surface of the Tsaoling landslide has dip direction and dip angle of 226° (from N clockwise) and 14°, respectively. Accelerations in the NE directions are favorable for triggering the landslide. There were three strong acceleration motions in that direction at 37 to 39 s after the generation of Chi-Chi earthquake, and our Newmark analysis revealed that the Tsaoling landslide was triggered by those seismic ground motions. Forecasting dangerous seismic ground motion based on measured frictional properties of landslide materials and on the information on existing active faults is important for mitigating earthquake-induced landslides.

(5) The centroids of the landslide mass and landslide deposits were determined accurately by using a GIS software and DTMs before and after the Chi-Chi earthquake. The vertical and horizontal displacements during the landslide were 524 m and 2524 m, respectively, which give an apparent friction coefficient of 0.21. This elevation difference and the landslide mass give the released potential energy $E_p$ of $1.6 \times 10^{15}$ J. The frictional work $E_f$ during the sliding of the landslide mass in Stages I and II before hitting the river bank was estimated at $3.6 \times 10^{14}$ J in the Newmark analysis with our Scenario 1 for semi-wet fault gouge data. This corresponds to about 23% of $E_p$, and the rest of $E_p$ must have

been consumed mostly during the stopping phase of the Tsaoling landslide after hitting the river bank in very complex processes such as fragmentation, heat dissipation, and spreading of the landslide deposits over a wide area. Analysis of particle size distribution of the landslide deposits would be of interest in estimating the energy used in the fragmentation.

## Acknowledgments

This research was funded by the National Science Council, Taiwan under the grants of NSC 102-2116-M-008-005 and NSC 99-2625-M-009-004-MY3. We thank the Editor, Guest Editors of this special issue, Prof. Theo van Asch and two anonymous reviewers for their useful and constructive reviews which greatly improved this paper.

## References

Beutner, E.C., Gerbi, G.P., 2005. Catastrophic emplacement of the Heart Mountain block slide, Wyoming and Montana, USA. Bull. Seismol. Soc. Am. 117, 724–735.
Bouchut, F., Westdickenberg, M., 2004. Gravity driven shallow water models for arbitrary topography. Commun. Math. Sci. 2, 359–389.
Boullier, A.M., Yeh, E.C., Boutareaud, S., Song, S.R., Tsai, C.H., 2009. Micro-scale anatomy of the 1999 Chi-Chi earthquake principal slip zone. Geochem. Geophys. Geosyst. 10, Q03016.
Boutareaud, S., Boullier, A.M., Andre'ani, M., Calugaru, D.G., Beck, P., Song, S.R., Shimamoto, T., 2010. Clay clast aggregates in gouges: new textural evidence for seismic faulting. J. Geophys. Res. 115, B02408.
Byerlee, J., 1978. Friction of rocks. Pure Appl. Geophys. 116, 615–626.
Campbell, C.S., 1989. Self-lubrication for long runout landslides. J. Geol. 97, 653–665.
Campbell, C.S., Cleary, P.W., Hopkins, M., 1995. Large-scale landslide simulations: global deformation, velocities and basal friction. J. Geophys. Res. Solid Earth 100, 8267–8283.
Chang, K.J., Taboada, A., Lin, M.L., Chen, R.F., 2005. Analysis of landsliding by earthquake shaking using a block-on-slope thermo-mechanical model: example of Jiufengershan landslide, central Taiwan. Eng. Geol. 80, 151–163.
Chang, K.J., Wei, S.K., Chen, R.F., Chan, Y.C., Tsai, P.W., Kuo, C.Y., 2013. Empirical modal decomposition of near field seismic signals of Tsaoling landslide. Earthquake-Induced Landslides. Springer, Berlin Heidelberg, pp. 421–430.
Chen, T.C., Lin, M.L., Hung, J.J., 2004. Pseudostatic analysis of Tsao-Ling rockslide caused by Chi-Chi earthquake. Eng. Geol. 71, 31–47.
Chen, R.F., Chan, Y.C., Angelier, J., Hu, J.C., Huang, C., Chang, K.J., Shih, T.Y., 2005. Large earthquake-triggered landslides and mountain belt erosion: the Tsaoling case, Taiwan. Compt. Rendus Geosci. 337, 1164–1172.
Chen, R.F., Chang, K.J., Angelier, J., Chan, Y.C., Deffontaines, B., Lee, C.T., Lin, M.L., 2006. Topographical changes revealed by high-resolution airborne LiDAR data: the 1999 Tsaoling landslide induced by the Chi-Chi earthquake. Eng. Geol. 88, 160–172.
Chen, T.C., Lin, M.L., Wang, K.L., 2014. Landslide seismic signal recognition and mobility for an earthquake-induced rockslide in Tsaoling, Taiwan. Eng. Geol. 171, 31–44.
Chigira, M., Wang, W.N., Furuya, T., Kamai, T., 2003. Geological causes and geomorphological precursors of the Tsaoling landslide triggered by the 1999 Chi-Chi earthquake, Taiwan. Eng. Geol. 68, 259–273.
Cleary, P.W., Campbell, C.S., 1993. Self-lubrication for long runout landslides: examination by computer simulation. J. Geophys. Res. Solid Earth 98, 21911–21924.
Crosta, G.B., Imposimato, S., Roddeman, D.G., 2003. Numerical modelling of large landslides stability and runout. Nat. Hazards Earth Syst. Sci. 3, 523–538.
Davies, T.R., McSaveney, M.J., 2009. The role of rock fragmentation in the motion of large landslides. Eng. Geol. 109 (1), 67–79.
Di Toro, G., Hirose, T., Nielsen, S., Pennacchioni, G., Shimamoto, T., 2006. Natural and experimental evidence of melt lubrication of faults during earthquakes. Science 311, 647–649.
Di Toro, G., Han, R., Hirose, T., De Paola, N., Nielsen, S., Mizoguchi, K., Ferri, F., Cocco, M., Shimamoto, T., 2011. Fault lubrication during earthquakes. Nature 471, 494–498.
Donath, F.A., Parker, R.B., 1964. Folds and folding. Geol. Soc. Am. Bull. 75, 45–62.
Dong, J.J., Lee, W.R., Lin, M.L., Huang, A.B., Lee, Y.L., 2009. Effects of seismic anisotropy and geological characteristics on the kinematics of the neighboring Jiufengershan and Hungtsaiping landslides during Chi-Chi earthquake. Tectonophysics 466, 438–457.
Dong, J.J., Yang, C.M., Yu, W.L., Lee, C.T., Miyamoto, Y., Shimamoto, T., 2013. Velocity–displacement dependent friction coefficient and the kinematics of giant landslide. In: Ugai, K., Yagi, H., Wakai, A. (Eds.), Earthquake-Induced Landslides. Springer, pp. 395–401.
Ferri, F., Di Toro, G., Hirose, T., Shimamoto, T., 2010. Evidence of thermal pressurization in high-velocity friction experiments on smectite-rich gouges. Terra Nova 22, 347–353.
Ferri, F., Di Toro, G., Hirose, T., Han, R., Noda, H., Shimamoto, T., Quaresimin, M., de Rossi, N., 2011. Low-to high-velocity frictional properties of the clay-rich gouges from the slipping zone of the 1963 Vaiont slide, northern Italy. J. Geophys. Res. Solid Earth 116, B09208.
Han, R., Hirose, T., 2012. Clay-clast aggregates in fault gouge: an unequivocal indicator of seismic faulting at shallow depths? J. Struct. Geol. 43, 92–99.
Han, R., Shimamoto, T., Hirose, T., Ree, J.H., Ando, J., 2007. Ultra-low friction of carbonate faults caused by thermal decomposition. Science 316, 878–881.
Hart, M.W., 2000. Bedding-parallel shear zones as landslide mechanisms in horizontal sedimental rocks. Environ. Eng. Geosci. 6 (5), 95–113.
Heim, A., 1932. Bergsturz und Menschenleben. Fretz und Wasmuth, Zürich.
Hirose, T., Shimamoto, T., 2005. Growth of molten zone as a mechanism of slip weakening of simulated faults in gabbro during frictional melting. J. Geophys. Res. 110, B05202.
Huang, C.C., Lee, Y.H., Liu, H.P., Keefer, D.K., Jibson, R.W., 2001. Influence of surface-normal ground acceleration on the initiation of the Jih-Feng-Erh-Shan landslide during the 1999 Chi-Chi, Taiwan, Earthquake. Bull. Seismol. Soc. Am. 91 (5), 953–958.
Hung, J.J., 1982. Investigation of engineering geology in the Tsaoling landslide. Report of rock mechanics tests, COA, 71-1.3-12(3), (in Chinese).
Hung, J.J., 2000. Chi-Chi earthquake induced landslides in Taiwan. Earthq. Eng. Eng. Seismol. 2, 25–33.
Hung, J.J., Lee, C.T., Lin, M.L., 2002. Tsao-ling rockslides, Taiwan. Catastrophic landslides: effects, occurrence, and mechanisms. Geol. Soc. Am. Rev. Eng. Geol. 15, 91–115.
Hungr, O., 1995. A model for the runout analysis of rapid flow slides, debris flows, and avalanches. Can. Geotech. J. 32, 610–623.
Hungr, O., Evans, S.G., 1996. Rock avalanche run out prediction using a dynamic model. Proc., 7th Int. Symp. Landslides 1, Trondheim, Norway, pp. 233–238.
Hungr, O., Evans, S.G., 2004. Entrainment of debris in rock avalanches: an analysis of a long run-out mechanism. Geol. Soc. Am. Bull. 116, 1240–1252.
Hungr, O., Evans, S.G., Bovis, M.J., Hutchinson, J.N., 2001. A review of the classification of landslides of the flow type. Environ. Eng. Geosci. 7, 221–238.
Jibson, R.W., Keefer, D.K., 1993. Analysis of the seismic origin of landslides: examples from the New Madrid seismic zone. Geol. Soc. Am. Bull. 105, 521–536.
Keefer, D.K., Wilson, R.C., 1989. Predicting earthquake-induced landslides with emphasis on arid and semi-arid environments. In: Sadler, P.M., Morton, D.M. (Eds.), Landslides in a Semi-arid Environment: Riverside. California. Inland Geological Society. 2, pp. 118–149.
Kuo, C.Y., Tai, Y.C., Bouchut, F., Mangeney, A., Pelanti, M., Chen, R.F., Chang, K.J., 2009. Simulation of Tsaoling landslide, Taiwan, based on Saint Venant equations over general topography. Eng. Geol. 104, 181–189.
Kuo, C.Y., Wei, S.K., Tsai, P.W., 2013. Ensemble empirical mode decomposition with supervised cluster analysis. Adv. Adapt. Data Anal. 5, 1350005.
Lee, C.N., 2001. Preliminary Study on the Tsaoling Landslide Area Under Earthquake. (Master's thesis) Institute of Civil Engineering, National Taiwan University.
Lee, C.T., 2011. Geomorphological evolution and geology of the Tsaoling rockslide. J. Chin. Soil Water Conserv. 42, 63–73.
Lee, C.T., 2012. Engineering Challenges and Countermeasures of the Difficult Geological Conditions in Taiwan. 2012 Taiwan Rock Engineering Symposium, pp. 29–36.
Lee, W.H.K., Shin, T.C., Kuo, K.W., Chen, K.C., Wu, C.F., 2001. CWB free-field strong-motion data from the 21 September Chi-Chi, Taiwan, earthquake. Bull. Seismol. Soc. Am. 91, 1370–1376.
Legros, F., 2002. The mobility of long-runout landslides. Eng. Geol. 63, 301–331.
Liao, C.J., Lee, D.H., Wu, J.H., Lai, C.Z., 2011. A new ring-shear device for testing rocks under high normal stress and dynamic conditions. Eng. Geol. 122, 93–105.
Miyamoto, Y., Shimamoto, T., Togo, T., Dong, J.J., Lee, C.T., 2009. Dynamic weakening of bedding-parallel fault gouge as a possible mechanism for catastrophic Tsaoling landslide induced by 1999 Chi-Chi earthquake. The Next Generation of Research on Earthquake-induced Landslides: An International Conference in Commemoration of 10th Anniversary of the Chi-Chi Earthquake, pp. 398–401.
Mizoguchi, K., Hirose, T., Shimamoto, T., Fukuyama, E., 2007. Reconstruction of seismic faulting by high-velocity friction experiments: an example of the 1995 Kobe earthquake. Geophys. Res. Lett. 34, L01308.
Newmark, N.M., 1965. Effects of earthquakes on dams and embankments. Geotechnique 15, 139–159.
Pirulli, M., Mangeney, A., 2008. Results of back-analysis of the propagation of rock avalanches as a function of the assumed rheology. Rock Mech. Rock. Eng. 41 (1), 59–84.
Romeo, R., 2000. Seismically induced landslide displacements: a predictive model. Eng. Geol. 58, 337–351.
Sawai, M., Shimamoto, T., Togo, T., 2012. Reduction in BET surface area of Nojima fault gouge with seismic slip and its implication for the fracture energy of earthquakes. J. Struct. Geol. 38, 117–138.
Scheidegger, A.E., 1975. Physical Aspects of Natural Catastrophes. Elsevier, (289 pp.).
Sepúlveda, S.A., Murphy, W., Jibson, R.W., Petley, D.N., 2005. Seismically induced rock slope failures resulting from topographic amplification of strong ground motions: the case of Pacoima Canyon, California. Eng. Geol. 80 (3–4), 336–348.
Shimamoto, T., Tsutsumi, A., 1994. A new rotary-shear high-speed frictional testingmachine: its basic design and scope of research. J. Struct. Geol. 39, 65–78.
Sosio, R., Crosta, G.B., Hungr, O., 2008. Complete dynamic modeling calibration for the Thurwieser rock avalanche (Italian Central Alps). Eng. Geol. 100, 11–26.
Tang, C.L., Hu, J.C., Lin, M.L., Angelier, J., Lu, C.Y., Chan, Y.C., Chu, H.T., 2009. The Tsaoling landslide triggered by the Chi-Chi earthquake, Taiwan: insights from a discrete element simulation. Eng. Geol. 106, 1–19.
Tanner, P.W.G., 1989. The flexural-slip mechanism. J. Struct. Geol. 11, 635–655.
Tanner, P.W.G., 1992. Morphology and geometry of duplexes formed during flexural-slip folding. J. Struct. Geol. 14 (10), 1173–1192.
Tika, T.E., Hutchinson, J.N., 1999. Ring shear tests on soil from the Vaiont landslide slip surface. Geotechnique 49, 59–74.
Togo, T., Shimamoto, T., 2012. Energy partition for grain crushing in quartz gouge during subseismic to seismic fault motion: an experimental study. J. Struct. Geol. 38, 139–155.
Togo, T., Shimamoto, T., Ma, S., Hirose, T., 2011. High-velocity frictional behavior of Longmenshan fault gouge from Hongkou outcrop, Sichuan, China and its implications for dynamic weakening of fault during the 2008 Wenchuan earthquake. Earthq. Sci. 24, 267–281.
Togo, T., Shimamoto, T., Dong, J.J., Lee, C.T., Yang, C.M., 2014. Triggering and runaway processes of catastrophic Tsaoling landslide induced by the 1999 Taiwan Chi-Chi

earthquake, as revealed by high-velocity friction experiments. Geophys. Res. Lett. 41 (6), 1907–1915.
Towhata, I., Yamazaki, H., Kanatani, M., Lin, C.E., Oyama, T., 2001. Laboratory shear tests of rock specimens collected from site of Tsao-ling earthquake-induced landslide. Tamkang J. Sci. Eng. 4, 209–219.
Tsutsumi, A., Shimamoto, T., 1996. Frictional properties of monzodiorite and gabbro during seismogenic fault motion. Geol. Soc. Jpn. 102, 240–248.
Tsutsumi, A., Shimamoto, T., 1997. High-velocity frictional properties of gabbro. Geophys. Res. Lett. 24, 699–702.
Ujiie, K., Tsutsumi, A., 2010. High-velocity frictional properties of clay-rich fault gouge in a megasplay fault zone, Nankai subduction zone. Geophys. Res. Lett. 37, L24310.
Voight, B., Faust, C., 1982. Frictional heat and strength loss in some rapid landslides. Geotechnique 32, 43–54.
Wang, W.N., Wu, H.L., Nakamura, H., Wu, S.C., Ouyang, S., Yu, M.F., 2003. Mass movements caused by recent tectonic activity: the 1999 Chi-chi earthquake in central Taiwan. Island Arc 12, 325–334.
Warr, L.N., Cox, S.J., 2001. Clay mineral transformations and weakening mechanisms along the Alpine Fault, New Zealand. In: Holdsworth, et al. (Eds.), The Nature and Significance of Fault Zone WeakeningGeol. Soc. Lond., Spec. Publ. 186, 85–101.
Weissel, J.K., Stark, C.P., 2001. Landslides triggered by the 1999 Mw7.6 Chi Chi earthquake in Taiwan and their relationship to topography. Geoscience and Remote Sensing Symposium, 2001. IGARSS'01. IEEE 2001 International. 2, pp. 759–761.
Wieczorek, G.F., Wilson, R.C., Harp, E.L., 1985. Map showing slope stability during earthquake in San Mateo County, California. Miscellaneous Investigation Maps I-1257-E, United States Geological Survey.
Wilson, R.C., Keefer, D.K., 1983. Dynamic analysis of a slope failure from the 6 August 1979 Coyote Lake, California, earthquake. Bull. Seismol. Soc. Am. 73, 863–877.
WRA, 2000. The Report: Remediation of Tsaoling Landslide. Water Resources Agency, Ministry of Economic Affairs, Taiwan, (in Chinese).
Wu, J.H., Chen, C.H., 2009. Back calculating the seismic shear strengths of the Tsaoling landslide associated with accelerograph and GPS data. Iran. J. Sci. Technol. Trans. B Eng. 33, 301–311.
Wu, J.H., Chen, C.H., 2011. Application of DDA to simulate characteristics of the Tsaoling landslide. Comput. Geotech. 38, 741–750.
Wu, J.H., Tsai, P.H., 2011. New dynamic procedure for back-calculating the shear strength parameters of large landslides. Eng. Geol. 123 (1–2), 129–147.
Yano, K., Shimamoto, T., Oohashi, K., Dong, J.J., Lee, C.T., 2009. Ultra-low friction of shale and clayey fault gouge at high velocities: implication for Jiufengershan landslide induced by 1999 Chi-Chi earthquake. The Next Generation of Research on Earthquake-induced Landslides: An International Conference in Commemoration of 10th Anniversary of the Chi-Chi Earthquake, pp. 402–406.
Yao, L., Ma, S., Shimamoto, T., Togo, T., 2013a. Structures and high-velocity frictional properties of the Pingxi fault zone in the Longmenshan fault system, Sichuan, China, activated during the 2008 Wenchuan earthquake. Tectonophysics 599, 135–156.
Yao, L., Shimamoto, T., Ma, S., Han, R., Mizoguchi, K., 2013b. Rapid postseismic strength recovery of Pingxi fault gouge from the Longmenshan fault system: experiments and implications for the mechanisms of high-velocity weakening of faults. J. Geophys. Res. Solid Earth 118, 1–17.